

# Multiscale adaptive PolSAR image superpixel generation based on local iterative clustering and polarimetric scattering features

Nengcai Li <sup>a</sup>, Deliang Xiang <sup>a</sup>\*, Xiaokun Sun <sup>a</sup>, Canbin Hu <sup>a</sup>, Yi Su <sup>b</sup>

<sup>a</sup> College of Information Science and Technology, Beijing University of Chemical Technology, Beijing, 100029, China

<sup>b</sup> College of Electronic Science and Technology, National University of Defense Technology, Changsha, 410073, China



## ARTICLE INFO

### Keywords:

Polarimetric Synthetic Aperture Radar (PolSAR)  
Simple Linear Iterative Clustering (SLIC)  
Multiscale superpixel  
Polarimetric scattering features

## ABSTRACT

Superpixel generation is an essential preprocessing step for intelligent interpretation of object-level Polarimetric Synthetic Aperture Radar (PolSAR) images. The Simple Linear Iterative Clustering (SLIC) algorithm has become one of the primary methods for superpixel generation in PolSAR images due to its advantages of minimal human intervention and ease of implementation. However, existing SLIC-based superpixel generation methods for PolSAR images often use distance measures based on the complex Wishart distribution as the similarity metric. These methods are not ideal for segmenting heterogeneous regions, and a single superpixel generation result cannot simultaneously extract coarse and fine levels of detail in the image. To address this, this paper proposes a multiscale adaptive superpixel generation method for PolSAR images based on SLIC. To tackle the issue of the complex Wishart distribution's inaccuracy in modeling urban heterogeneous regions, this paper employs the polarimetric target decomposition method. It extracts the polarimetric scattering features of the land cover, then constructs a similarity measure for these features using Riemannian metric. To achieve multiscale superpixel segmentation in a single superpixel segmentation process, this paper introduces a new method for initializing cluster centers based on polarimetric homogeneity measure. This initialization method assigns denser cluster centers in heterogeneous areas and automatically adjusts the size of the search regions according to the polarimetric homogeneity measure. Finally, a novel clustering distance metric is defined, integrating multiple types of information, including polarimetric scattering feature similarity, power feature similarity, and spatial similarity. This metric uses the polarimetric homogeneity measure to adaptively balance the relative weights between the various similarities. Comparative experiments were conducted using three real PolSAR datasets with state-of-the-art SLIC-based methods (Qin-RW and Yin-HLT). The results demonstrate that the proposed method provides richer multiscale detail information and significantly improves segmentation outcomes. For example, with the AIRSAR dataset and the step size of 42, the proposed method achieves improvements of 16.56% in BR and 12.01% in ASA compared to the Qin-RW method. Source code of the proposed method is made available at [https://github.com/linengcai/PolSAR\\_MS\\_ASILC.git](https://github.com/linengcai/PolSAR_MS_ASILC.git).

## 1. Introduction

Synthetic Aperture Radar (SAR), as an active microwave sensor, enables all-weather, all-day earth observation without being affected by cloud cover and sunlight. Compared to SAR, PolSAR can obtain richer back-scatter information, making it highly attractive for both military and civilian applications (Li et al., 2023b; Zhang et al., 2024a). PolSAR image segmentation, as a fundamental issue in the field of intelligent interpretation of PolSAR images, is an important part of PolSAR image understanding. Existing PolSAR image segmentation algorithms can be divided into two categories: pixel-level methods and object-level methods (Zou et al., 2020). Pixel-level methods treat image pixels as

the basic processing unit, and traditional pixel-level approaches primarily rely on pixel features and statistical information. Recently, deep learning methods have achieved excellent results in optical image processing; however, due to their requirement for large amounts of labeled data, the development of deep learning in PolSAR image processing is still in its infancy (Garg et al., 2021). While pixel-level methods can effectively preserve detailed information in images, their computational efficiency is relatively low when processing high-resolution images. Additionally, the speckle noise inherent in PolSAR images can greatly affect the accuracy of PolSAR image segmentation algorithms. In contrast, object-level PolSAR image segmentation methods have the advantages of higher computational efficiency and reduced sensitivity

\* Corresponding author.

E-mail address: [xiangdeliang@buct.edu.cn](mailto:xiangdeliang@buct.edu.cn) (D. Xiang).

to speckle noise. These methods can integrate rich features from local regions, such as edges, textures, shapes, and spatial relationships with neighboring targets, thus gaining increasing attention.

Superpixel segmentation algorithm is an essential preprocessing step for object-level PolSAR image intelligent interpretation. It can generate highly homogeneous and compact image segments that adhere well to boundaries, thereby preserving target information. Consequently, they are widely applied in region extraction (Zhang et al., 2024b), image classification (Shi et al., 2023; Guo et al., 2022), target detection (Sun et al., 2023; Deng et al., 2024), and time-series monitoring (Ye et al., 2022; Xu et al., 2023).

### 1.1. Related work in superpixel generation

Existing superpixel segmentation algorithms can be roughly divided into two categories: graph-based algorithms and gradient ascent-based algorithms (Barcelos et al., 2024). Graph-based algorithms treat pixels as graph nodes and assign weights to the edges between nodes. Then, they use preset segmentation criteria to partition the graph into superpixels. Representative algorithms of this category include the Normalized Cuts algorithm (Shi and Malik, 2000) and the Superpixel Lattices algorithm (Moore et al., 2008). These algorithms typically use global optimization methods to ensure the overall consistency of superpixel segmentation. However, this results in high computational complexity and relatively difficult implementation. On the other hand, gradient ascent-based algorithms start from a rough initial clustering, and refine the clustering through iterative optimization until convergence criteria are met to form superpixels. Representative algorithms in this category include the Mean Shift algorithm (Comaniciu and Meer, 2002), the Quick Shift algorithm (Vedaldi and Soatto, 2008), the Watersheds method (Vincent and Soille, 1991), the Turbopixel algorithm (Levinshtein et al., 2009), and the SLIC algorithm (Achanta et al., 2012). These algorithms generally offer high computational efficiency and generate regular superpixels, making them suitable as preprocessing steps for image interpretation algorithms.

The SLIC algorithm is widely developed and applied to PolSAR images due to its minimal human intervention and ease of implementation. Feng et al. (2014) introduced the Wishart distance as a similarity measure to replace the color distance in the original SLIC algorithm, utilizing the contextual information provided by superpixels to enhance classification performance. Qin et al. (2014) introduced the Revised Wishart (RW) distance to measure similarity between regions, and improved SLIC's initialization and post-processing steps. Additionally, they used the traditional Constant False Alarm Rate (CFAR) edge detector (Schou et al., 2003) instead of gradient calculation in optical images. Song et al. (2015) adopted the Bartlett distance as a measure of distance in PolSAR data, effectively improving computational efficiency. Recently, Yin et al. (2021) integrated four classic PolSAR image statistical distances into the enhanced clustering function. Among these, the Hotelling-Lawley Trace (HLT) distance and the Symmetric Revised Wishart (SRW) distance were employed in the SLIC algorithm for the first time. This integration enables a comprehensive comparison and evaluation of feature similarity in PolSAR images. Li et al. (2022) proposed a novel cross-iteration strategy that integrates the advantages of the revised Wishart distance and geodesic distance with higher computational efficiency. Later, Li et al. (2023c) introduced a new strategy to establish a relationship between the initial superpixel size and the structural complexity of PolSAR images. Additionally, they adopted the determinant ratio test distance to construct the clustering distance metric. These researches are all based on the Wishart distribution assumption, a model well-suited for distributed targets and effective in describing the backscatter from natural areas. However, research has shown that urban heterogeneous areas can render the Wishart distribution inapplicable, and non-Gaussian clutter modeling can accurately describe such heterogeneous areas (Greco and Gini, 2007). Consequently, Xiang et al. (2017) introduced the Spherically Invariant

Random Vector (SIRV) product model and constructed the symmetric SIRV distance, and then redesigned edge detector and SLIC distance function. Compared to methods based on the Wishart distribution, this approach achieves better segmentation results in heterogeneous regions. Furthermore, they introduced a polarimetric homogeneity measure to adaptively balance the weights between spatial similarity and feature similarity, ensuring the generation of regular and compact superpixels in homogeneous regions. For time-series monitoring tasks, Xie et al. (2015) derived the Wishart distance between two interferometric coherence matrices, thereby developing a SLIC-based superpixel generation method for dual-temporal PolSAR images. Gao et al. (2021) proposed a root mean square-based time-series polarimetric similarity measure to assess the polarimetric similarity between time-series data. They also used the adaptive weighting factor introduced by Xiang et al. (2017) to balance feature similarity and spatial similarity, thereby extending the SLIC superpixel generation method to time-series data.

### 1.2. Related work in polarimetric target decomposition

The polarimetric target decomposition method is a typical approach for extracting polarimetric scattering features from PolSAR data. Based on physical models, this method decomposes the coherence matrix or covariance matrix into a weighted sum of possible scattering mechanisms of the land cover. The origin of these methods is the three-component decomposition method proposed by Freeman and Durden (Freeman and Durden, 1998). Subsequently, some studies have refined decomposition processes based on existing scattering models through mathematical optimizations, such as polarimetric orientation angle compensation (Yamaguchi et al., 2011) and helix angle compensation (An et al., 2016). Other studies have introduced novel detailed scattering models to achieve an accurate and comprehensive description of the polarimetric coherence matrix. For instance, Singh and Yamaguchi (2018) proposed the compounded scattering model, which explains the possible compounded dipole forms of the helix scattering model. They also introduced the oriented dipole model and the oriented quarter-wave reflectors model.

In recent years, numerous new polarimetric target decomposition methods have been proposed. Quan et al. (2023a) described the cross scattering model using a planar structure distribution, thereby constructing a roll-invariant cross polarization scattering model. Moreover, they designed a refined decomposition method based on a root-discrimination-based parameter inversion strategy, enabling a fully physical interpretation of matrix elements. Li et al. (2023a) constructed three generalized scattering models by introducing three independent polarimetric orientation angles, achieving a detailed interpretation of land cover scattering. Hu et al. (2023), based on the rotated dihedral model and polarimetric asymmetry, introduced a novel urban revised rate to mitigate the overestimation of volume scattering in urban areas through a power transfer strategy. Hu et al. (2024) improved the existing generalized surface, double-bounce, and volume scattering models to propose a general three-component PolInSAR target decomposition framework, comparing the performance of three generalized volume scattering models within this framework.

The polarimetric target decomposition method based on physical models can accurately perceive changes in land cover scattering mechanisms. This makes it widely applicable in scenarios such as land use and cover monitoring (Quan et al., 2023b; Parida and Mandal, 2020), disaster monitoring (Ge et al., 2020), and change detection (Silva-Perez et al., 2021; Alonso et al., 2020), demonstrating its potential for constructing similarity measures.

### 1.3. Motivation and contribution of this paper

The aforementioned PolSAR superpixel segmentation studies have experimented with different distance metrics for PolSAR data to replace the color distance in the SLIC algorithm for optical images. These

distance metrics based on statistical models typically yield optimal results only when their physical assumptions are met. To address the issue that the Wishart distribution assumption is not suitable for urban heterogeneous areas, this paper employs the polarimetric target decomposition method to extract the polarimetric scattering features of the land cover. Then, a similarity measure for polarimetric scattering features is constructed to replace the traditional statistical distance.

In addition, the effectiveness of superpixel segmentation directly impacts the performance of subsequent image intelligent interpretation methods, and this effectiveness largely depends on the selection of the segmentation scale. In PolSAR images, the significant size disparity between natural homogeneous regions and the targets of interest makes it difficult for a single superpixel segmentation scale to balance the accurate segmentation of small targets with the over-segmentation of the overall image. To extract multiscale detail information from images, some studies manually determine multiple superpixel numbers and repeatedly apply the superpixel generation algorithm, resulting in pyramid segmentation outcomes ranging from coarse to fine (Zhang et al., 2017; Shi and Pun, 2019; Wang et al., 2024). However, these approaches are computationally inefficient. Other methods first generate small size superpixels and then achieve the final segmentation through region merging (Liu et al., 2016; Xiang et al., 2019). However, these methods have high implementation complexity and the resulting superpixels are no longer uniformly shaped.

Inspired by the aforementioned research, this paper proposes a multiscale adaptive superpixel generation method based on SLIC for PolSAR images. This method enables multiscale information extraction within a single superpixel segmentation process and achieves excellent segmentation results in both homogeneous and heterogeneous regions. The key aspects of this method include the construction of the polarimetric scattering feature similarity measure and the multiscale initialization of clustering centers. The polarimetric scattering feature similarity measure is used for edge map generation and the novel multi-feature adaptive distance metric. The main contributions of this paper are as follows:

- **Polarimetric Scattering Feature Similarity Measure:** A novel similarity measure based on polarimetric scattering features is proposed, which replaces traditional statistical distances. This measure effectively captures the variations in scattering mechanisms, enhancing the accuracy of edge detection and superpixel segmentation, especially in urban heterogeneous regions.
- **Multiscale Initialization of Clustering Centers Based on Polarimetric Homogeneity Measure:** A new method for initializing clustering centers is proposed, which deploys more initial clustering centers in heterogeneous regions and allows for adaptive adjustment of the search area sizes based on the polarimetric homogeneity measure. This approach ensures a balanced distribution of clustering centers and enables multiscale information extraction.
- **Multi-feature Adaptive Clustering Distance Metric:** Combining the polarimetric scattering feature similarity measure and power similarity measure, a composite feature similarity measure is defined. An adaptive weighting factor based on the polarimetric homogeneity measure is introduced to balance the relative weights between composite feature similarity and spatial similarity. Finally, a multi-feature adaptive distance metric is defined, ensuring compact and regular superpixel generation in homogeneous regions while accurately capturing the edges and shapes of targets in heterogeneous regions.

By addressing the limitations of existing methods and introducing innovative approaches for similarity measurement and clustering center initialization, this paper advances the state-of-the-art in superpixel generation for PolSAR images. The rest of this paper is organized as follows. Section 2 introduces the definition of the polarimetric scattering feature similarity measure. Section 3 presents the multiscale adaptive

superpixel generation method, including the new edge detector, the multiscale initialization of clustering centers, and the definition of the SLIC distance metric. Section 4 lists the experimental results on three real PolSAR datasets, along with an analysis of these results. Conclusion is provided in Section 5.

## 2. Polarimetric scattering feature similarity measure construction based on polarimetric target decomposition

### 2.1. Polarimetric scattering features extraction based on polarimetric target decomposition

The PolSAR system measures the polarimetric scattering matrix  $S$ , which contains information about the scatterers. The elements in  $S$  are represented as follows:

$$S = \begin{bmatrix} S_{HH} & S_{HV} \\ S_{VH} & S_{VV} \end{bmatrix}. \quad (1)$$

The element  $S_{XY}$  in the matrix represents the complex scattering coefficient, where the subscript X indicates the receive polarization and Y indicates the transmit polarization. Further, H represents horizontal polarization, and V represents vertical polarization. For multi-look PolSAR images, it is generally assumed that the system follows the reciprocity principle, i.e.,  $S_{HV} = S_{VH}$ . The scattering information of the target is represented using the polarimetric coherence matrix  $T$ , which is defined as

$$T = \frac{1}{L} \sum_{l=1}^L p_l p_l^H \quad (2)$$

where

$$p_l = \frac{\sqrt{2}}{2} [S_{HH} + S_{VV}, S_{HH} - S_{VV}, 2S_{HV}]^T. \quad (3)$$

The  $L$  represents the number of looks,  $(\cdot)^H$  denotes the Hermitian operator, and  $(\cdot)^T$  denotes the matrix transpose operation. The polarimetric coherence matrix  $T$  and the polarimetric covariance matrix  $C$  can be converted into each other through the following unitary transformation:

$$C = Q^T T Q, T = Q C Q^T \quad (4)$$

where the unitary matrix  $Q$  is defined as

$$Q = \frac{1}{\sqrt{2}} \begin{bmatrix} 1 & 0 & 1 \\ 1 & 0 & -1 \\ 0 & \sqrt{2} & 0 \end{bmatrix}. \quad (5)$$

The purpose of polarimetric target decomposition is to decompose the original polarimetric coherence matrix into a weighted sum of several specific scattering mechanisms:

$$T_{ori} = \sum_{i=1}^N P_i T_i \quad (6)$$

where  $N$  is the number of scattering components in the polarimetric target decomposition method,  $T_i$  represents a specific polarimetric scattering model, and  $P_i$  is the polarimetric scattering power corresponding to the polarimetric scattering model  $T_i$ . The classical Freeman three-component decomposition (Freeman and Durden, 1998) is based on the models of volume scattering, surface scattering, and double-bounce scattering. Due to the number of variables is less than the number of equations, certain assumptions need to be made during the polarimetric decomposition process. This results in ignoring some equations and consequently leads to a certain degree of information loss. The six-component decomposition method we previously proposed (Li et al., 2023a) introduces three independent polarimetric orientation angles, constructing three refined scattering models. These six models fully explain the nine elements of the polarimetric coherence matrix, making comprehensive use of the information contained within the matrix.

Therefore, we adopt this six-component polarimetric target decomposition method, which decomposes the polarimetric coherence matrix into the simplified surface scattering model  $\mathbf{T}_s$ , the improved double-bounce scattering model  $\mathbf{T}_d$ , the generalized quarter-wave model  $\mathbf{T}_{od}$ , the generalized dipole model  $\mathbf{T}_q$ , the volume scattering model  $\mathbf{T}_v$ , and the helix scattering model  $\mathbf{T}_h$ :

$$\mathbf{T}_s = \begin{bmatrix} 1 & 0 & 0 \\ 0 & 0 & 0 \\ 0 & 0 & 0 \end{bmatrix}, \quad (7)$$

$$\mathbf{T}_d = \begin{bmatrix} 0 & 0 & 0 \\ 0 & \cos^2 2\theta_d & \cos 2\theta_d \sin 2\theta_d \\ 0 & \cos 2\theta_d \sin 2\theta_d & \sin^2 2\theta_d \end{bmatrix}, \quad (8)$$

$$\mathbf{T}_{od} = \frac{1}{2} \begin{bmatrix} 1 & \cos 2\theta_{od} & \sin 2\theta_{od} \\ \cos 2\theta_{od} & \cos^2 2\theta_{od} & \cos 2\theta_{od} \sin 2\theta_{od} \\ \sin 2\theta_{od} & \cos 2\theta_{od} \sin 2\theta_{od} & \sin^2 2\theta_{od} \end{bmatrix}, \quad (9)$$

$$\mathbf{T}_q = \frac{1}{2} \begin{bmatrix} 1 & j \cos 2\theta_q & j \sin 2\theta_q \\ -j \cos 2\theta_q & \cos^2 2\theta_q & \cos 2\theta_q \sin 2\theta_q \\ -j \sin 2\theta_q & \cos 2\theta_q \sin 2\theta_q & \sin^2 2\theta_q \end{bmatrix}, \quad (10)$$

$$\mathbf{T}_v = \frac{1}{4} \begin{bmatrix} 2 & 0 & 0 \\ 0 & 1 & 0 \\ 0 & 0 & 1 \end{bmatrix}, \quad (11)$$

$$\mathbf{T}_h = \frac{1}{2} \begin{bmatrix} 0 & 0 & 0 \\ 0 & 1 & \pm j \\ 0 & \mp j & 1 \end{bmatrix}. \quad (12)$$

Here,  $\theta_d$ ,  $\theta_{od}$ , and  $\theta_q$  are the independent polarimetric orientation angle parameters introduced for the improved double-bounce scattering model, the generalized quarter-wave model, and the generalized dipole model, respectively. After polarimetric decomposition, the polarimetric scattering features of the polarimetric coherence matrix is extracted as

$$\mathbf{F} = [P_s, P_d, P_{od}, P_q, P_v, P_h, \mathbf{T}_s, \mathbf{T}_d, \mathbf{T}_{od}, \mathbf{T}_q, \mathbf{T}_v, \mathbf{T}_h]^T. \quad (13)$$

## 2.2. Construction of polarimetric scattering feature similarity measure

The similarity measurement between pixels in PolSAR images is crucial for SLIC superpixel generation. On one hand, this similarity measurement will be applied to compute the edge map; on the other hand, it will serve as one of the feature information components in the clustering distance metric. Many studies assume that PolSAR data follows a specific probability distribution, such as the commonly used Wishart distribution, and calculate the similarity between PolSAR data using methods such as maximum likelihood estimation or hypothesis testing (Qin et al., 2022). However, there is not yet a recognized perfect mathematical probability model suitable for all scenes of PolSAR data. In this paper, we avoid assuming a probability distribution model for PolSAR data. Instead, we extract the polarimetric scattering features of the land cover using polarimetric target decomposition, and then use these features to construct the similarity measurement.

In some studies, the polarimetric scattering features extracted using polarimetric target decomposition method have been utilized to identify changes in land cover (Silva-Perez et al., 2021; Alonso et al., 2020). These studies typically employ ratio or norm distances to measure the differences in polarimetric scattering power  $P_i$ , reflecting actual changes in the land cover. In these studies, the polarimetric scattering models  $\mathbf{T}_i$  are used only during polarimetric target decomposition process and do not participate in the similarity computation, resulting in some information loss. In this research, we leverage the complete polarimetric scattering features information  $\mathbf{F}$  to reconstruct the polarimetric coherence matrix:

$$\mathbf{T}_{rec} = \sum_i k_i P_i \mathbf{T}_i, i = s, d, od, q, v, h. \quad (14)$$

Here,  $k_i$  is the weight coefficient corresponding to the scattering model  $\mathbf{T}_i$ . This parameter can be assigned a higher weight for scattering components that are of greater interest in the study. For example, when researching urban areas, the coefficient for the double-bounce scattering component can be increased, whereas when studying forested regions, the coefficient for the volume scattering component can be elevated. It can be readily shown that, in the case where the volume scattering component is non-zero, the reconstructed matrix is Hermitian symmetric positive definite (SPD).

After reconstructing the polarimetric coherence matrix, we employ the geodesic distance based on Riemannian manifolds to describe the similarity between two reconstructed matrices. The geodesic distance corresponds to the shortest distance between two points along the curvature of the manifold. For SPD matrices, the classical Riemannian metrics include the affine invariant Riemannian metric (AIRM) (Pennec et al., 2006), Kullback–Leibler divergence metric (KLDM) (Moakher and Batchelor, 2006), and Jensen–Bregman LogDet divergence metric (JBLD) (Cherian et al., 2012). Their definitions are as follows:

$$D_{AIRM}(\mathbf{A}, \mathbf{B}) = \left\| \log \left( \mathbf{A}^{-\frac{1}{2}} \mathbf{B} \mathbf{A}^{-\frac{1}{2}} \right) \right\|_F, \quad (15)$$

$$D_{KLDM}(\mathbf{A}, \mathbf{B}) = \frac{1}{2} (\mathbf{A}^{-1} \mathbf{B} + \mathbf{B}^{-1} \mathbf{A} - 2\mathbf{I}), \quad (16)$$

$$D_{JBLD}(\mathbf{A}, \mathbf{B}) = \log \left| \frac{\mathbf{A} + \mathbf{B}}{2} \right| - \frac{1}{2} \log |\mathbf{AB}|. \quad (17)$$

Here,  $\mathbf{A}$  and  $\mathbf{B}$  represent two SPD matrices,  $\mathbf{I}$  is the identity matrix of the same shape as  $\mathbf{A}$  and  $\mathbf{B}$ ,  $\log(\cdot)$  denotes the natural logarithm,  $\|\cdot\|_F$  is the Frobenius norm, and  $|\cdot|$  represents the determinant of the matrix.

Eq. (15) has the lowest computational efficiency because it requires eigenvalue and matrix logarithm calculations, making it less commonly applied in PolSAR similarity computations. Although Eq. (16) does not require eigenvalue and matrix logarithm calculations, it involves matrix inversion, which can slow down computation and potentially lead to instability. Cherian et al. (2012) demonstrated that in some cases,  $D_{KLDM}$  may overestimate the Riemannian metric. Additionally, it can be shown that the  $D_{KLDM}$  is mathematically equivalent to the SRW distance. Classical statistical distances such as the revised Wishart distance and HLT distance also require the computation of matrix inverses, while the distance metric defined in Eq. (17) only requires the computation of matrix determinants. By leveraging the Cholesky decomposition, the determinant of SPD matrices can be calculated efficiently, making the distance metric defined in Eq. (17) the most computationally efficient. This distance metric retains the inversion invariance and affine invariance properties of  $D_{AIRM}$ , while also exhibiting non-negativity, definiteness, inverse invariance, and symmetry, and satisfying the triangle inequality. Experimental results in Cherian et al. (2012) demonstrate that the computational speed is significantly improved without any decrease in accuracy. Thus, this paper adopts  $D_{JBLD}$  as the distance metric between the two reconstructed matrices. The resulting polarimetric scattering feature similarity measure has the following advantages:

1. Compared to distance metrics based on probability distribution models, the polarimetric scattering features extracted through the polarimetric target decomposition method can directly reflect the actual scattering mechanisms of the land cover. The similarity measure constructed using these features is less influenced by land cover homogeneity, providing a intuitive and accurate description of differences.
2. Current algorithms for change detection based on polarimetric target decomposition typically utilize only the polarimetric scattering power  $P_i$  to construct similarity measures. In contrast, the proposed similarity measure leverages the complete set of polarimetric scattering features  $\mathbf{F}$ , resulting in a more comprehensive use of information.

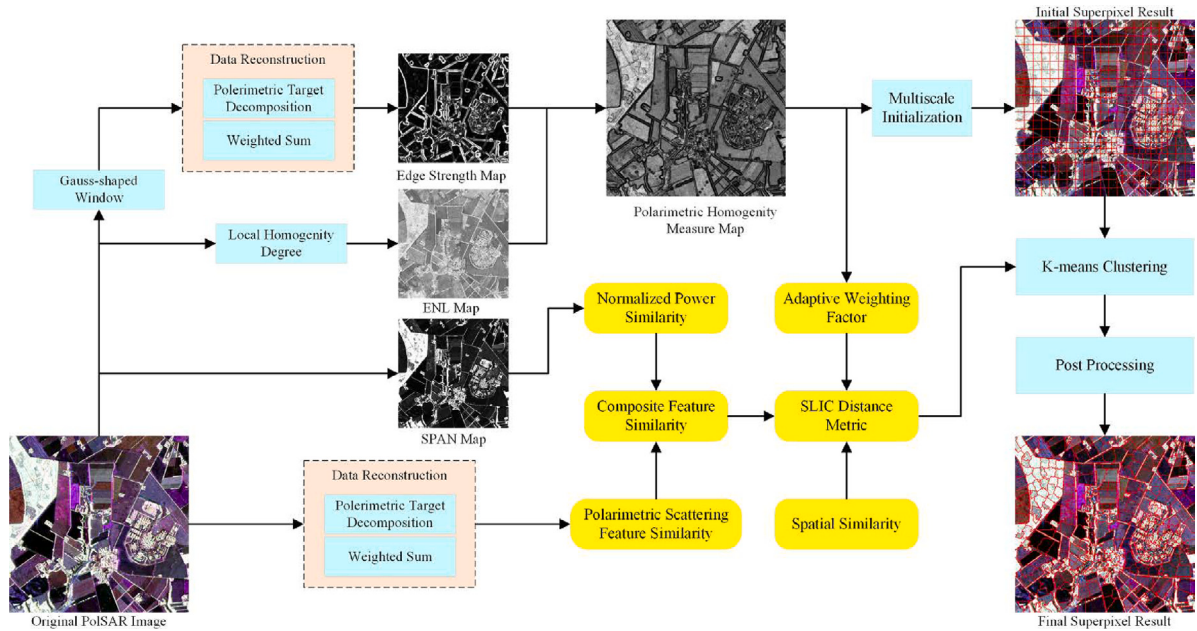


Fig. 1. Overall flow chart of the proposed algorithm.

3. The scattering model weight coefficients  $k_i$  in the polarimetric scattering feature similarity measure can be adjusted according to the type of land cover of interest, enabling flexible and targeted application in subsequent tasks.

### 3. Multiscale adaptive PolSAR superpixel generation

The SLIC superpixel generation algorithm is generally divided into three parts: (1) initialization of cluster centers; (2) local K-means clustering; (3) post-processing. This paper follows this framework, and the overall implementation process is shown in Fig. 1. The key improvements of our method lie in the edge detector, multiscale initialization clustering center method, and the novel multi-feature adaptive clustering function. These will be described in detail below.

#### 3.1. Edge detector

For PolSAR images, Schou et al. (2003) designed the classical CFAR edge detector based on a hypothesis test assuming equality of the covariance matrices under the complex Wishart distribution. The CFAR edge detector employs a rectangular window filter, whose structure is shown in Fig. 2(a). The shape of this window is determined by its length  $l_f$ , width  $w_f$ , spacing  $d_f$ , and orientation  $\theta_f$ . All pixels within the rectangular window have equal weights. Based on the CFAR edge detector framework, some studies have improved the similarity measure by assuming different statistical distributions for PolSAR data (Xiang et al., 2017; Liu et al., 2014). Other studies have focused on improving the filtering window (Xiang et al., 2017; Shui and Cheng, 2012), giving higher weights to pixels closer to the edges. Shui and Cheng (2012) demonstrated that the strong speckle noise in SAR images causes the rectangular filter to contain some unwanted high-frequency components, which may result in false local maxima near true edges and thus form false edges.

A Gauss-shaped filter can effectively overcome this defect. The structure of the Gauss-shaped filter is shown in Fig. 2(b). Unlike the rectangular filter where all pixels have equal weights, in the Gauss-shaped filter, pixels closer to the centerline have higher weights. The horizontal Gauss-shaped window function is defined as

$$W(x, y) = \frac{1}{\sqrt{2\pi}\sigma_x\sqrt{2\pi}\sigma_y} \exp\left(-\left(\frac{x^2}{2\sigma_x^2} + \frac{y^2}{2\sigma_y^2}\right)\right) \quad (18)$$

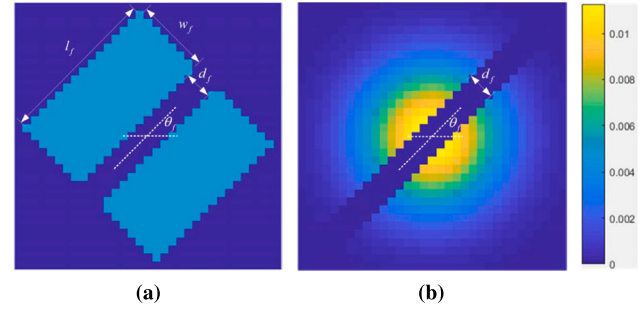


Fig. 2. Filter structure: (a) Rectangular filter; (b) Gauss-shaped Filter.

where  $\sigma_x$  and  $\sigma_y$  control the weight decay rate of the window in the length and width directions, respectively. The Gauss-shaped window with orientation angle  $\theta_f$  can be obtained by rotating Eq. (18) like

$$W^{\theta_f}(x, y) = W(x \cos \theta_f - y \sin \theta_f, x \sin \theta_f + y \cos \theta_f). \quad (19)$$

Using Eq. (19), the average coherence matrices for the regions on both sides of the centerline can be calculated as

$$\hat{T}_i = \frac{\sum_{(x,y) \in \Omega_i} W^{\theta_f}(x, y) T(x, y)}{\sum_{(x,y) \in \Omega_i} W(x, y)}, i = 1, 2 \quad (20)$$

where  $\Omega_i (i = 1, 2)$  represents the pixel sets of the two regions on either side of the center line. After this, the polarimetric scattering features are extracted using the six-component decomposition method we proposed earlier (Li et al., 2023a), and data reconstruction is performed using Eq. (14). Finally, the similarity of the regions on both sides of the centerline is calculated using the distance metric from Eq. (17). The complete edge detection algorithm is shown in Algorithm 1.

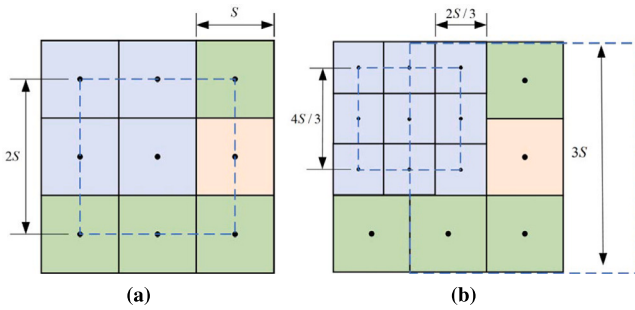
#### 3.2. Multiscale initialization method for cluster centers

As shown in Fig. 3(a), the superpixel generation algorithm based on SLIC typically distributes the initial cluster centers uniformly across the entire image at regular network steps  $S$ . Then, the cluster centers are then moved to the lowest gradient position in the  $3 \times 3$  neighborhood. During the iterative clustering process, similar pixels

**Algorithm 1** Edge Detection Algorithm Based on Polarization Target Decomposition

**Begin**

- 1: Set the filter parameters  $\sigma_x$ ,  $\sigma_y$ ,  $d_f$ ,  $\theta_f$ , and the scattering component weight coefficients  $k_i (i = 1, 2, \dots, N)$ .
- 2: For  $N_f = \pi/\theta_f$  different directional filter windows, calculate the Gauss-shaped weight matrix and compute the average coherence matrix for the regions on both sides of the centerline using Eq. (20).
- 3: Perform polarization target decomposition on the average coherence matrix and reconstruct the data using Eq. (14).
- 4: Calculate the polarization scattering feature similarity metric  $D_{JBLD}$  for each direction using Eq. (17).
- 5: Identify the maximum distance  $D_{\max}$  among the  $N_f$  directions and its corresponding direction  $\theta_{\max}$ .
- 6: Save the distance  $D_{\max}$  and direction  $\theta_{\max}$ , then move to the next pixel and repeat from step 2.

**End**


**Fig. 3.** Distribution of cluster centers: (a) Square distribution; (b) Refinement distribution based on polarimetric homogeneity measure. The blue areas represent heterogeneous regions, the orange areas represent homogeneous regions, and the green areas represent other regions. (For interpretation of the references to color in this figure legend, the reader is referred to the web version of this article.)

are searched within a  $2S \times 2S$  neighborhood around the superpixel centers. This initialization method can generate superpixels of approximately equal size and prevent clustering centers from being seeded on noisy pixels. However, in PolSAR images, natural homogeneous regions usually occupy large areas, and the targets of interest are generally small. Therefore, it is challenging to select a suitable step size that can effectively segment small targets without excessive segmentation. To address this issue, this paper proposes a multiscale initialization method for cluster centers based on polarimetric homogeneity measure.

The polarimetric homogeneity measure is defined as the ratio between local homogeneity and edge strength, where local homogeneity is represented by the equivalent number of looks (ENL). ENL is an important parameter in the statistical modeling of multi-look PolSAR images. Anfinsen et al. (2009) provides a method for estimating ENL that is less affected by texture. Assuming that the random matrix  $Z$  is a semi-positive definite matrix and follows a Wishart distribution with degrees of freedom  $L$  and scale matrix  $\Sigma = E\{Z\}/L$ . The determinant of matrix  $Z$  is defined as

$$E\{\text{tr}(ZZ)\} = L^2\text{tr}(\Sigma\Sigma) + L\text{tr}(\Sigma)^2 \quad (21)$$

where  $\text{tr}(\cdot)$  denotes the trace of the matrix. Based on Eq. (21), ENL is estimated as

$$\text{ENL} = \frac{\text{tr}(\Sigma)^2}{\langle \text{tr}(XX) \rangle - \text{tr}(\Sigma\Sigma)} \quad (22)$$

where  $X = Z/L$ , and  $\langle \cdot \rangle$  denotes the sample average. The ENL is larger in homogeneous regions and smaller in heterogeneous regions. In contrast, edge strength is smaller in homogeneous regions and larger in heterogeneous regions. By utilizing the opposing trends of these

two factors, they can more effectively distinguish between homogeneous and heterogeneous areas, leading to the development of the polarimetric homogeneity measure:

$$\text{HM} = \frac{\text{ENL}}{\text{EDGE}} \quad (23)$$

where EDGE represents the edge map calculated using Algorithm 1. Utilizing the characteristic that the HM can significantly distinguish between homogeneous and heterogeneous regions, we designed a multiscale initialization method for cluster centers. As shown in Fig. 3(b), this method places more cluster centers in heterogeneous regions, thereby effectively reducing under-segmentation in these areas. Additionally, it adaptively adjusts the size of the clustering search space based on the average HM of the region where the cluster center is located. The detailed description of this method is provided in Algorithm 2.

**Algorithm 2** Multi-Scale Initialization Method Based on Polarimetric Homogeneity Measure

**Begin**

- 1: Set parameters  $S$ ,  $\sigma_{\text{homo}}$ , and  $\sigma_{\text{hete}}$ , where  $\sigma_{\text{homo}}$  is the proportion for homogeneous regions and  $\sigma_{\text{hete}}$  is the proportion for heterogeneous regions.
- 2: Uniformly distribute the initial superpixels across the entire image with a step size of  $S$ .
- 3: Use mean filter of size  $2S \times 2S$  to traverse the entire HM map with a step size of  $2S$  from left to right and top to bottom, obtaining a list representing the average HM of regions.
- 4: Sort this list in ascending order, setting the regions corresponding to the top  $\sigma_{\text{hete}}$  of elements as heterogeneous regions and the regions corresponding to the bottom  $\sigma_{\text{homo}}$  of elements as homogeneous regions.
- 5: Redistribute the initial cluster centers in heterogeneous regions using the method shown in Fig. 3(b), setting the search space for cluster centers located in heterogeneous regions to  $\frac{4}{3}S \times \frac{4}{3}S$ , in homogeneous regions to  $3S \times 3S$ , and in other regions to  $2S \times 2S$ .
- 6: Iterate through all cluster centers and move each center to the lowest edge strength location within a  $3 \times 3$  neighborhood.

**End**

### 3.3. Multi-feature adaptive clustering distance metric

The multi-feature adaptive clustering distance metric in this paper integrates polarimetric scattering feature similarity, normalized power similarity, and spatial similarity. The definition of polarimetric scattering feature similarity has been provided earlier. This similarity measures the distance between two reconstructed matrices using the Jensen–Bregman LogDet divergence metric  $D_{JBLD}$ . The total scattering power SPAN describes the overall echo power from land cover. SPAN varies with land cover types. It is highest in building areas, followed by vegetation areas, while bare soil and water bodies have lower values. Thus, differences in SPAN effectively capture variations in land cover and changes in image texture. The globally normalized total scattering power similarity is given by

$$D_P = \frac{|\text{SPAN}(x_i, y_i) - \text{SPAN}(x_j, y_j)|}{\max(\text{SPAN})} \quad (24)$$

where SPAN is calculated using the trace of the original polarimetric coherence matrix, with  $(x_i, y_i)$  representing the spatial coordinates of the pixel. To enhance the ability to describe differences in land cover scattering features, this paper integrates normalized power similarity  $D_P$  with polarimetric scattering feature similarity  $D_{JBLD}$  to obtain composite feature similarity  $D_F$ :

$$D_F = (1 + D_P) \cdot D_{JBLD}. \quad (25)$$

When power differences are significant,  $(1 + D_P)$  provides a maximum gain of up to 2.

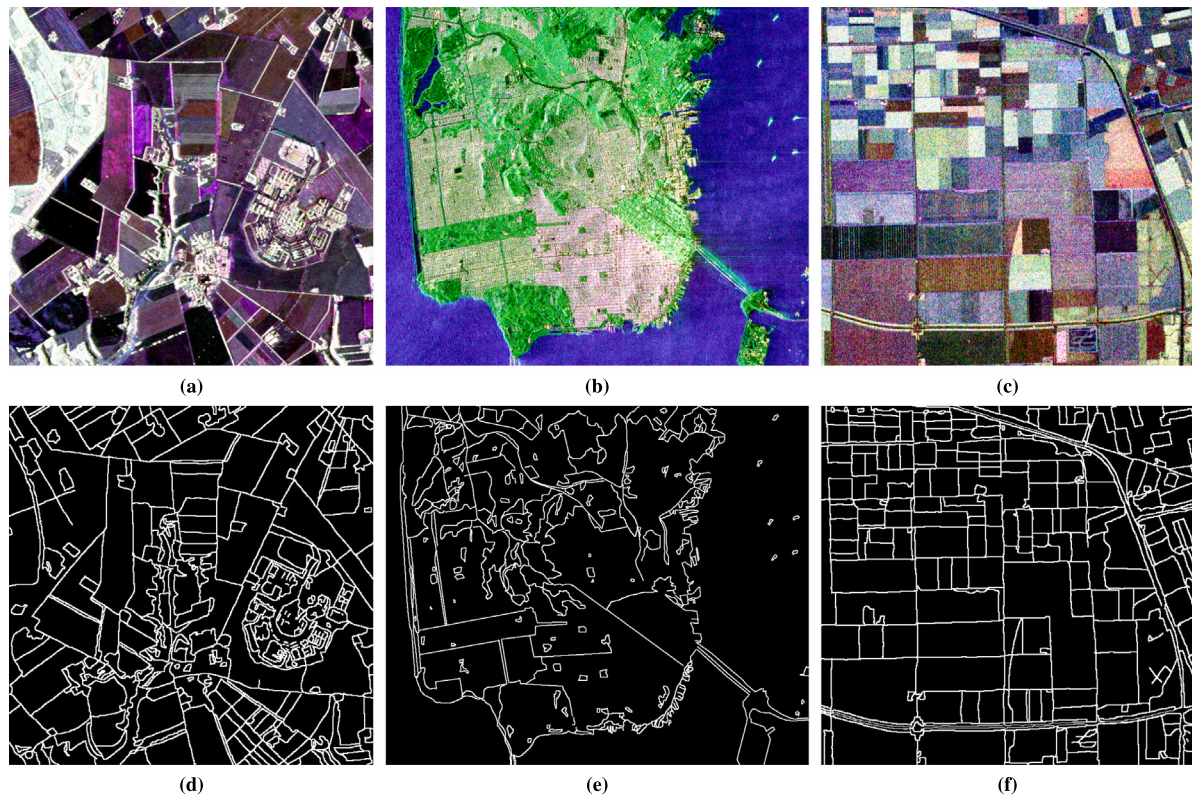


**Fig. 4.** Experimental data Pauli coded images and corresponding ground truth edges: (a) and (d) GF-3 C-band data; (b) and (e) AIRSAR L-band data; (c) and (f) EMISAR L-band data.

Spatial similarity is used to describe the distance between pixels and cluster centers, thereby ensuring the compactness of superpixels:

$$D_S = \sqrt{(x_i - x_j)^2 + (y_i - y_j)^2}. \quad (26)$$

To adaptively balance the relative weights between spatial similarity  $D_S$  and composite feature similarity  $D_F$ , this paper introduces an adaptive weight factor based on the polarimetric homogeneity measure:

$$\beta_{\text{adp}} = \beta \cdot \frac{1}{2} (HM(x_i, y_i) + HM(x_j, y_j)) \quad (27)$$

where  $\beta$  is a constant manually set through trial and error. In this paper's experiments,  $\beta$  is set to 1. Finally, the multi-feature adaptive clustering distance metric is defined as

$$D_{SLIC} = \sqrt{(D_F)^2 + \beta_{\text{adp}} \cdot (D_S/S_{sp})^2} \quad (28)$$

where  $S_{sp}$  represents the side length of the search area corresponding to the cluster center, determined during the initialization of the cluster centers.  $S_{sp}$  is used to normalize spatial similarity. In homogeneous regions, the weight factor  $\beta_{\text{adp}}$  is high, making spatial similarity dominant and resulting in compact superpixels. In heterogeneous regions, the weight factor  $\beta_{\text{adp}}$  is low, making feature similarity dominant and allowing the superpixels to better adhere to the image edges.

#### 4. Experiment and analysis

##### 4.1. Experiment dataset, evaluation metrics and experimental parameter settings

As shown in Fig. 4, extensive experiments were conducted on three real PolSAR datasets to verify the effectiveness of the proposed algorithm. Figs. 4(a)–4(c) are Pauli coded images, and Figs. 4(d)–4(f) are their corresponding ground truth edges.

**EMISAR L-band Data:** As shown in Fig. 4(a), this dataset was collected by the EMISAR L-band system over Foulum, Denmark. The image size is  $589 \times 598$ , with azimuth and range resolutions of 0.75 m and 1.45 m, respectively. The main land cover types in this data are agricultural areas, but the field edges are not as regular as those in the AIRSAR L-band data, and this dataset includes some dense buildings.

**GF-3 C-band Data:** As shown in Fig. 4(b), this dataset was acquired by the GF-3 C-band system over San Francisco, California, USA. The image size is  $765 \times 902$ , with azimuth and range resolutions of 5.36 m and 2.25 m, respectively. This data includes typical land covers such as ocean, urban buildings, and forest.

**AIRSAR L-band Data:** As shown in Fig. 4(c), this dataset was collected by NASA/JPL's AIRSAR L-band system over Flevoland, Netherlands. The image size is  $581 \times 605$ , with azimuth and range resolutions of 12.1 m and 6.6 m, respectively. The main land cover types in this data are agricultural fields, with distinct edges between different crops.

Using the above three datasets, this paper first compares the performance of the CFAR edge detection method with the proposed edge detection method. It then analyzes the performance of the polarimetric homogeneity measure in different land cover areas. Following this, it presents a visual and quantitative comparison with two advanced PolSAR superpixel generation methods (Qin-RW method (Qin et al., 2014) and Yin-HLT method (Yin et al., 2021)). After that, experiments on three diverse large-scene PolSAR images were conducted to demonstrate the robustness of the proposed algorithm. Finally, ablation experiments are performed to verify the effectiveness of the multiscale initialization step.

Before conducting the experiments, some parameters need to be set. Firstly, this paper applies a  $3 \times 3$  mean filter to the images to reduce noise influence. Secondly, in the edge detection experiments, the CFAR edge detector's window shape parameters length  $l_f$ , width  $w_f$ , and spacing  $d_f$  are set to 11, 5, and 1, respectively, and the orientation  $\theta_f$  is set to  $\pi/8$ . To ensure a similar window area between different edge detection methods, the parameters  $d_f$  and  $\theta_f$  for the proposed edge

detector are kept consistent with the CFAR method, and parameters  $\sigma_x$  and  $\sigma_y$  are set to 3.1 and 1.55, respectively. Additionally, since this paper does not focus on a specific type of land cover, all parameters  $k_i$  in polarimetric scattering feature similarity are set to 1. Thirdly, in the multiscale initialization process, the proportion of homogeneous regions  $\sigma_{\text{homo}}$  is set to 20%, and the proportion of heterogeneous regions  $\sigma_{\text{hete}}$  is set to 10%. This leads to an increase of about 12.5% in the number of superpixels compared to other methods at the same initial step size  $S$ . Finally, for the iterative clustering process, the balance coefficient in this paper is determined adaptively. The balance coefficient  $m$  for the Qin-RW method is set to 1 according to Qin et al. (2014), and the balance coefficient  $m$  for the Yin-HLT method is set to 2 according to Yin et al. (2021).

To quantitatively evaluate the performance of different methods, this paper introduces two metrics to assess the segmentation results: Boundary Recall (BR) and Achievable Segmentation Accuracy (ASA) (Liu et al., 2011). BR is defined as the ratio of the number of superpixel boundary pixels within  $\epsilon$  pixels of any ground truth boundary pixel to the total number of ground truth boundary pixels. A higher BR indicates fewer missed true boundaries and better boundary adherence. BR is calculated using the following formula:

$$\text{BR} = \frac{\sum_{p \in B(g)} I(\min_{p \in B(s)} \|p - q\| < \epsilon)}{|B(g)|}. \quad (29)$$

Here,  $B(g)$  and  $B(s)$  represent the sets of ground truth boundary pixels and superpixel boundary pixels, respectively. The function  $I(\cdot)$  returns 1 when a superpixel boundary pixel is within a tolerance range  $\epsilon$  of a ground truth boundary pixel.  $|B(g)|$  represents the total number of ground truth boundary pixels. In this paper,  $\epsilon$  is set to 2.

ASA is the overlap ratio between superpixels and ground truth segmentation objects, which is defined as

$$\text{ASA} = \frac{\sum_k \max_i |s_k \cap g_i|}{\sum_i |g_i|} \quad (30)$$

where  $g_i$  represents the ground truth segmentation objects,  $s_k$  represents the segmentation objects from the superpixel algorithm, and  $|\cdot|$  denotes the size of the segmentation objects. A higher ASA value indicates a better match between superpixels and the objects in the PolSAR image.

#### 4.2. Performance of edge detector and polarimetric homogeneity measure

Fig. 5 shows the normalized edge strength maps of the CFAR method and the proposed edge detection method. Figs. 5(a)–5(c) are the results of CFAR, and Figs. 5(d)–5(f) are the results of the proposed method. Fig. 6 provides the enlarged views of the red rectangular areas in Fig. 5. Figs. 6(a) and 6(b) correspond to the enlarged views of the areas in Figs. 5(a) and 5(d), and 6(c) and 6(d) correspond to the enlarged views of the areas in Figs. 5(b) and 5(e). The comparison shows that CFAR can detect obvious edges, but overall, it performs worse than the proposed method. Firstly, the edge strength detected by the CFAR algorithm is very weak. This is because the distance metric based on the Wishart distribution cannot effectively distinguish two similar matrices, whereas the proposed polarimetric scattering feature similarity distinguishes land covers better by focusing on differences in scattering mechanisms. Secondly, for urban heterogeneous areas, as shown in Fig. 6, the proposed method can extract clear and rich edges in these areas, while the traditional CFAR algorithm extracts fewer and blurrier edges, and some false edges appear. This is because the complex Wishart distribution assumption is not suitable for urban heterogeneous areas, while the proposed method does not have this limitation. Additionally, the traditional CFAR method uses a rectangular bilater window, which leads to some false local maxima near true edges (Shui and Cheng, 2012). This phenomenon appears frequently in Figs. 6(a) and 6(c). In contrast, the Gauss-shaped window provides a smoother local mean estimation, making it more effective for edge

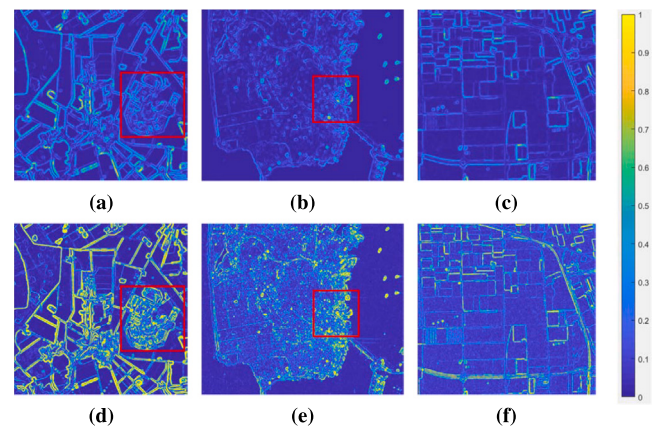


**Fig. 5.** Edge detection results: (a) CFAR — Gaofen-3; (b) CFAR — AIRSAR; (c) CFAR — EMISAR; (d) Proposed method — Gaofen-3; (e) Proposed method — AIRSAR; (f) Proposed method — EMISAR.

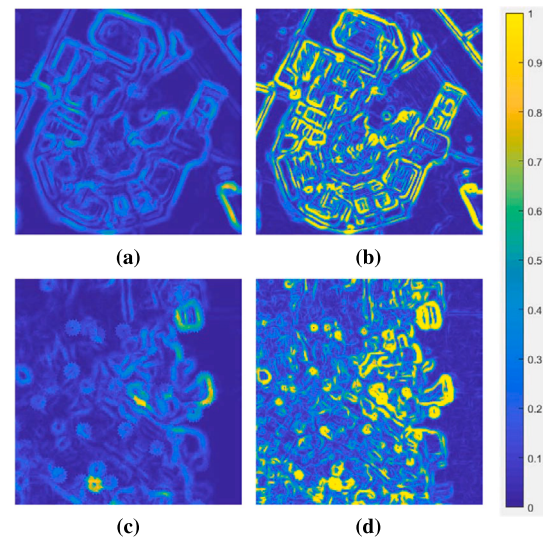


**Fig. 6.** Magnified edge detection results: (a), (b), (c), and (d) are the magnified results of the areas marked with red rectangle in Fig. 5(a), (d), (b), and (e), respectively. (For interpretation of the references to color in this figure legend, the reader is referred to the web version of this article.)

detection in small targets and urban heterogeneous areas compared to the rectangular window.

To intuitively evaluate the performance of the edge detectors, we selected two narrow strips from the edge results of the AIRSAR data and the EMISAR data, and plotted the edge strength line graphs for the two algorithms. For the strip selected from the AIRSAR data, as shown in Figs. 7(a) and 7(b), the proposed edge detector accurately detected four true edges, while the CFAR algorithm missed two edges. The strip selected from the EMISAR data is located in a dense building area. As shown in Figs. 7(c) and 7(d), the CFAR algorithm detected only the rightmost edge, while the proposed algorithm missed only one edge.

After computing the edge maps, Fig. 8 shows the polarimetric homogeneity measure maps for the three datasets. The results clearly distinguish between homogeneous and heterogeneous regions. This distinction helps in allocating more initial cluster centers in the heterogeneous regions of interest and adaptively determining the weighting factor in the clustering distance metric. Consequently, the superpixel generation algorithm achieves fine and accurate segmentation in heterogeneous regions, while the generated superpixels remain compact in homogeneous regions.

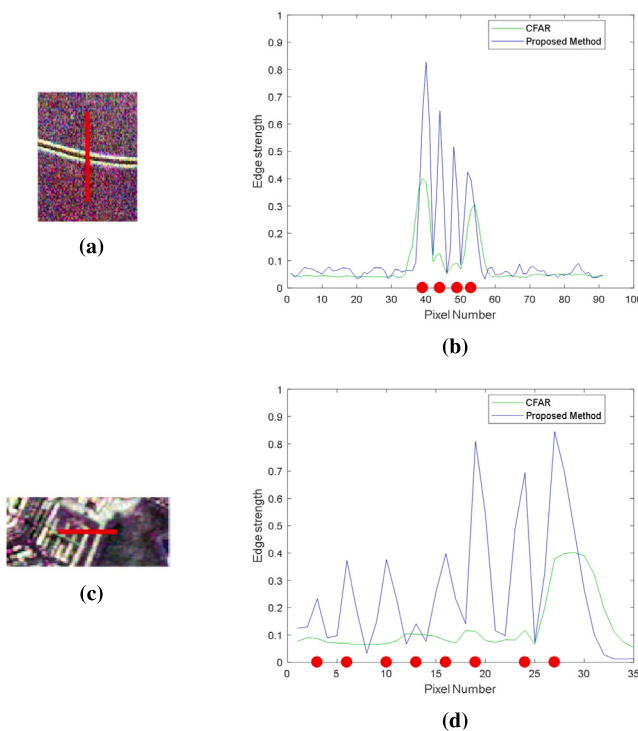


**Fig. 7.** Edge strength comparison of two detectors (red dots = true edge pixels): (a) Pauli image — stripe region, AIRSAR; (b) Line graphs — AIRSAR; (c) Pauli image — stripe region, EMISAR; (d) Line graphs — EMISAR. (For interpretation of the references to color in this figure legend, the reader is referred to the web version of this article.)

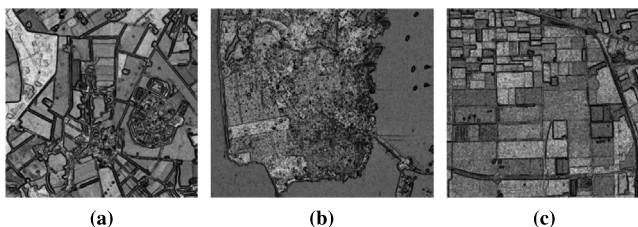


**Fig. 8.** Polarimetric homogeneity measure maps for different data: (a) Gaofen-3; (b) AIRSAR; (c) EMISAR.

#### 4.3. Performance of superpixel generation method

In this section, we compare the Qin-RW method (Qin et al., 2014), the Yin-HLT method (Yin et al., 2021), proposed method without the multiscale initialization step (ASLIC), and proposed complete method (MS-ASLIC) through visual comparisons and quantitative evaluations. The experimental results are detailed below.

##### 4.3.1. Superpixel generation results for EMISAR data

Fig. 9 shows the superpixel generation results of four methods on the EMISAR data with a step size of 28. In the first row, the images are obtained by overlaying red lines representing superpixel edges on the Pauli coded images. In the second row, each pixel's coherence matrix is replaced by the average value of the superpixel it belongs to, and then Pauli coding is applied. Firstly, comparing Figs. 9(a) to 9(d), it is visually evident that in homogeneous natural regions, the Yin-HLT method produces superpixels with rough edges and irregular shapes. On the contrary, the Qin-RW method and two proposed methods generate more regular superpixels with smoother edges. Secondly, observing the heterogeneous building area A marked with yellow ellipse in Figs. 9(e) to 9(h), it can be seen that the Qin-RW method retains the least detail in

the heterogeneous building area. The Yin-HLT method performs better than the Qin-RW method but has some obvious segmentation errors. The ASLIC method achieves better segmentation but is limited by the initial distribution of superpixels, failing to achieve finer segmentation for the details of heterogeneous regions. In contrast, the MS-ASLIC method retains the most edge information due to distributing more initial superpixels in texture-rich heterogeneous regions. Comparing the results of regions B and C marked with yellow ellipse in Figs. 9(e) to 9(h), it is found that neither the Qin-RW method nor the Yin-HLT method can segment these narrow strip-like regions accurately. However, the two methods proposed in this paper effectively retain these detailed information.

To compare the results in detail, the area D marked with yellow rectangle in Fig. 9 is enlarged and the results are plotted in Fig. 10. Notably, this area contains both homogeneous natural regions and irregularly shaped heterogeneous building areas, making it suitable for evaluating the superpixel methods' segmentation capabilities in different regions. It can be observed that all four methods achieve good segmentation results in the homogeneous regions. However, for the heterogeneous regions, such as the narrow strip area marked with yellow ellipse in Fig. 10(e), both the Qin-RW method and the Yin-HLT method perform poorly. In contrast, the two methods proposed in this paper retain the edge details of these narrow strips, and overall, the MS-ASLIC method preserves the most edge information. There are three main reasons for this result:

1. The polarimetric scattering feature similarity measure thoroughly distinguishes the differences in scattering mechanisms among different land covers, and the normalized power similarity amplifies these differences in a gain manner. Therefore, the proposed composite feature similarity  $D_F$  is better at describing the feature differences between different land covers compared to traditional Wishart distance measures such as RW distance and HLT distance.
2. The introduction of the adaptive weight factor based on the polarimetric homogeneity measure reduces the weight of spatial similarity in heterogeneous regions. This adjustment makes the generation of superpixels more inclined to feature similarity, resulting in better segmentation of small targets and ensuring that the segmentation results closely adhere to the real edges.
3. The multiscale initialization step brings more initial cluster centers to the heterogeneous regions, directly and effectively improving the segmentation results.

To quantitatively compare the performance of the four methods on the EMISAR data, we conducted experiments with different values of the step size  $S$ , where  $S = [42, 34, 28, 23, 19, 15, 12, 10]$ . Figs. 11(a) and 11(b) describe the BR and ASA performance of the four methods under different step sizes. Due to the multiscale initialization step increasing the superpixel number by approximately 12.5%, the horizontal axis is set to the number of superpixels rather than the step size for a fair comparison. It can be observed that the Yin-HLT method overall performs better than the Qin-RW method in terms of edge adhesion (BR). For the evaluation metric ASA, the Qin-RW method slightly outperforms the Yin-HLT method when the number of superpixels is less than 1500. When the number exceeds 2000, the results of the two methods converge to equal. The results in Fig. 9 also visually reflect that the Yin-HLT method is more sensitive to edges compared to the Qin-RW method. However, because the superpixels generated by the Yin-HLT method are irregular in shape, it is prone to segmentation errors, leading to poorer ASA performance. The BR and ASA of the proposed methods are better than the previous two methods, and the gap is more obvious when the number of superpixels is small. Additionally, a horizontal comparison of the two proposed methods shows that when the number of superpixels is less than 1000, the additional superpixels brought by the multiscale initialization step directly and effectively improve BR and ASA, especially under circumstances where too few superpixels lead to noticeable under-segmentation. This reflects the capability of the multiscale initialization step in extracting detailed information from the images.

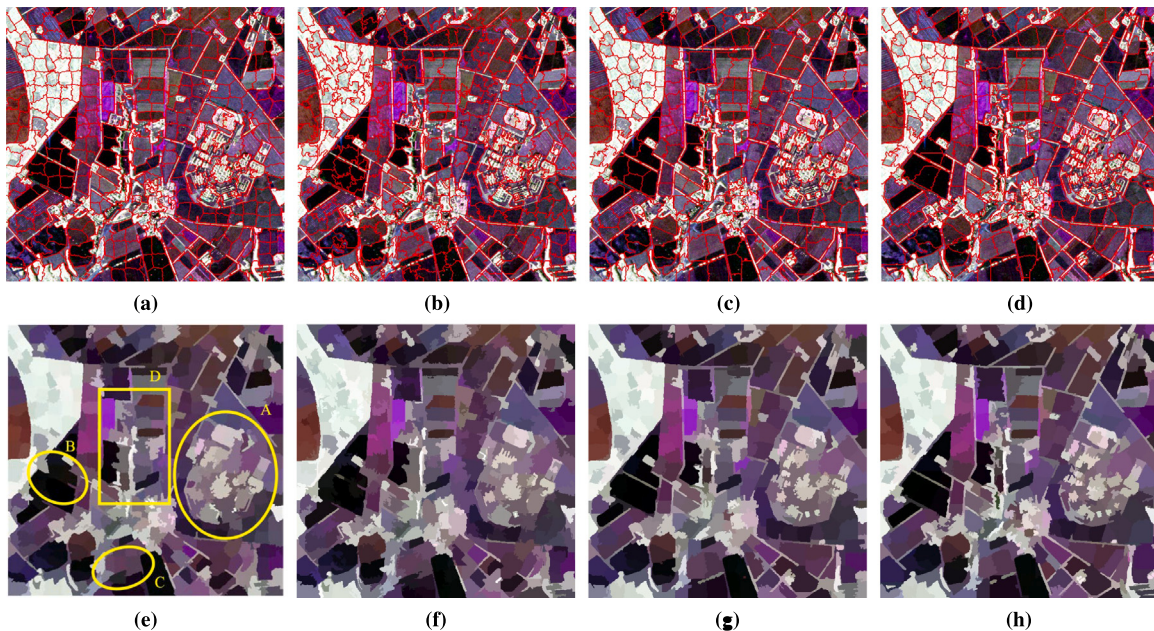


**Fig. 9.** Superpixel results of four methods when  $S = 28$ . The first row shows the superpixel images of different methods, with superpixel edges indicated by red lines. In the second row, the coherence matrix of each pixel is replaced by the average value of the superpixel to which it belongs. (a), (e) Qin-RW; (b), (f) Yin-HLT; (c), (g) ASLIC; (d), (h) MS-ASLIC. (For interpretation of the references to color in this figure legend, the reader is referred to the web version of this article.)

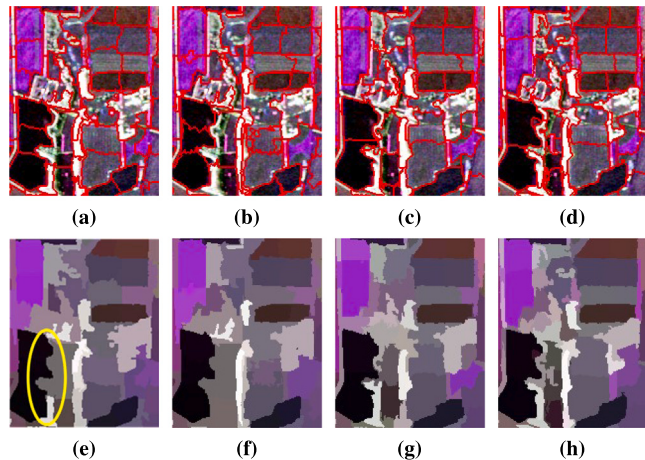


**Fig. 10.** Magnified superpixel generation results of the area marked with yellow square in Fig. 9. (a)–(h) correspond to (a)–(h) in Fig. 9, respectively. (For interpretation of the references to color in this figure legend, the reader is referred to the web version of this article.)

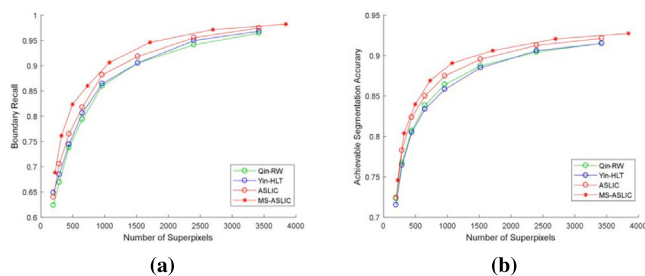


**Fig. 11.** Line graphs of evaluation metrics for four methods on EMISAR data at different numbers of superpixels: (a) BR; (b) ASA..

#### 4.3.2. Superpixel generation results for GF-3 data

Fig. 12 shows the results of the four methods on the GF-3 dataset with a step size  $S$  of 34. First, observing the region A marked with yellow ellipse in Fig. 12, it can be seen that when the step size  $S$  is larger than the target scale, both the Qin-RW and Yin-HLT methods fail to segment the ship targets on the sea, while the proposed methods effectively retain these small-scale details. Furthermore, Fig. 13 shows the segmentation results of the four methods for sea targets under different step sizes. It can be observed that the Qin-RW and Yin-HLT methods only when the step size is close to the ship target scale can they correctly segment the ship targets. In contrast, both of the proposed methods can completely and correctly segment all ship targets under all step sizes. For the bridge region B marker with yellow ellipse in Fig. 12, the Qin-RW and Yin-HLT methods show significant segmentation errors, while both proposed methods maintain the shape of the bridge well. In the region C marked with yellow rectangle, the Qin-RW and Yin-HLT methods confuse the boundaries between some urban building areas and forest vegetation areas, while the proposed methods produce straight boundaries that match the actual land covers. Observing the coastal region D marked with yellow rectangle, it can be seen that the Qin-RW method retains the least details, the Yin-HLT method retains more coastal edge details, and the proposed methods provide the most precise segmentation of the coastline. Additionally, comparing the two proposed methods, it is clear that the MS-ASLIC method achieves more detailed segmentation of coastal buildings and city buildings, resulting in more accurate outcomes. Overall, the Qin-RW method generates the most regular superpixels but retains the least details. The Yin-HLT method generates rough-edged superpixels that retain more image details but show some significant segmentation errors. The proposed methods offer superior segmentation results, with the MS-ASLIC method achieving the most detailed segmentation in complex scenes.

Using the same parameters as in Section 4.3.1, we set the step size to a range of different values for experimentation to quantitatively compare the performance of four methods on GF-3 data. The results are plotted in Fig. 14, it can be observed that the Qin-RW method performs the worst in terms of BR, significantly lower than the other methods. This is consistent with the results in Fig. 12. The Yin-HLT

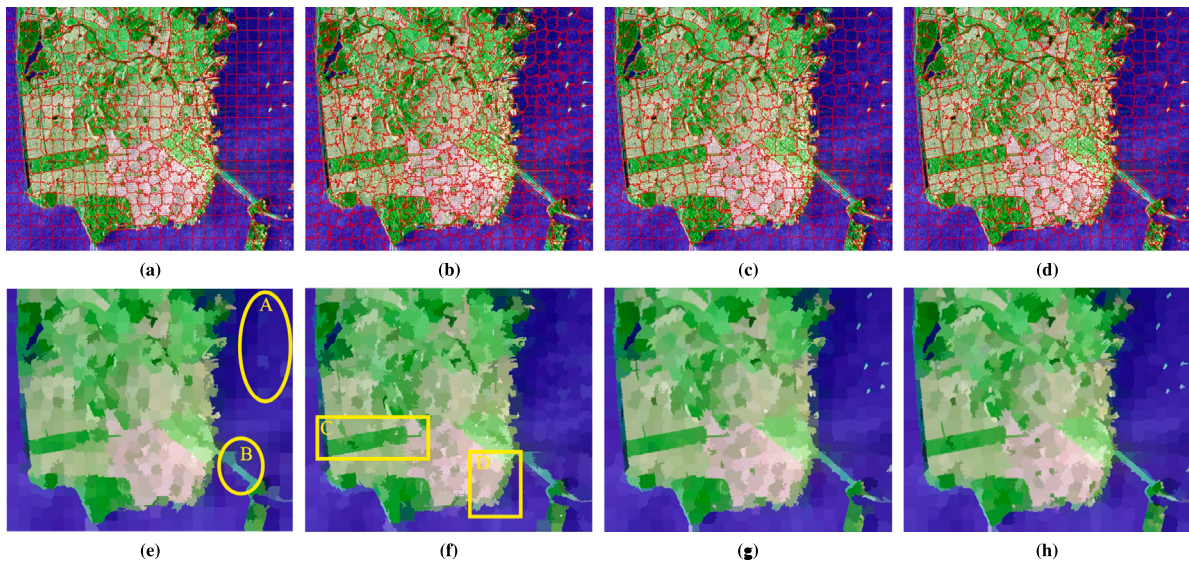


Fig. 12. Superpixel results of four methods on GF-3 data when  $S = 34$ . (a), (e) Qin-RW; (b), (f) Yin-HLT; (c), (g) ASLIC; (d), (h) MS-ASLIC.

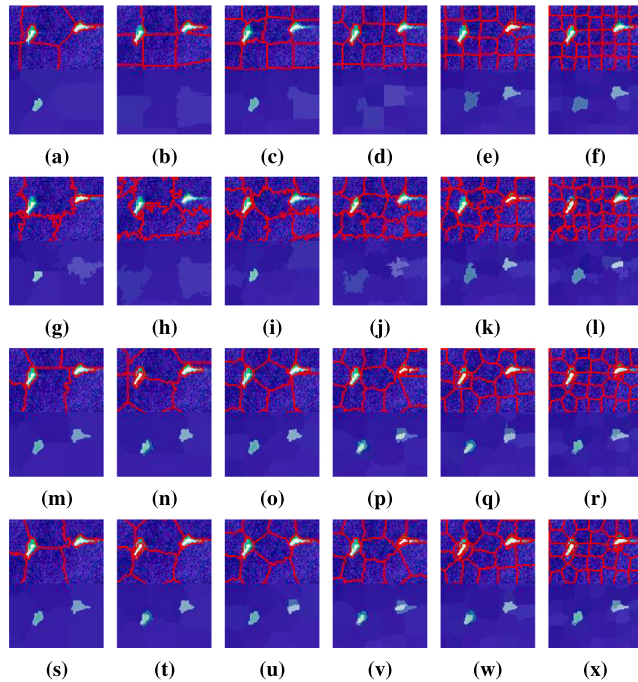


Fig. 13. Segmentation results of ship targets at different step sizes for four methods: (a)–(f) Qin-RW; (g)–(l) Yin-HLT; (m)–(r) ASLIC; (s)–(x) MS-ASLIC. Step sizes from left to right: 42, 34, 28, 23, 19, 15.

method performs the worst in terms of ASA, indicating that the Yin-HLT method resulted in the most segmentation errors. Compared to the Yin-HLT method, the ASLIC method does not greatly improve the edge adherence index (BR) but significantly improves ASA, thus reducing the segmentation errors. Additionally, it can be observed that the multiscale initialization method significantly improves BR and ASA when the number of superpixels is low, and the MS-ASLIC method achieves the best performance in both BR and ASA.

#### 4.3.3. Superpixel generation results for AIRSAR data

Fig. 15 shows the results of the four methods on AIRSAR data with a step size of 19. Because the step size is smaller than the size of the cultivated land in the image, a rough observation indicates that

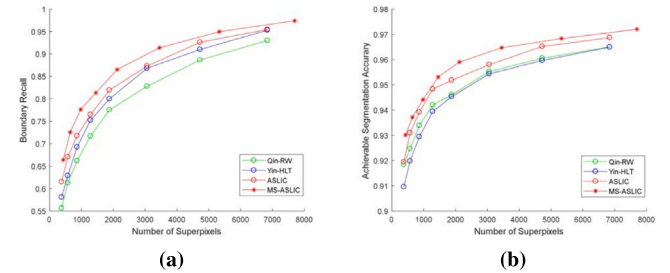
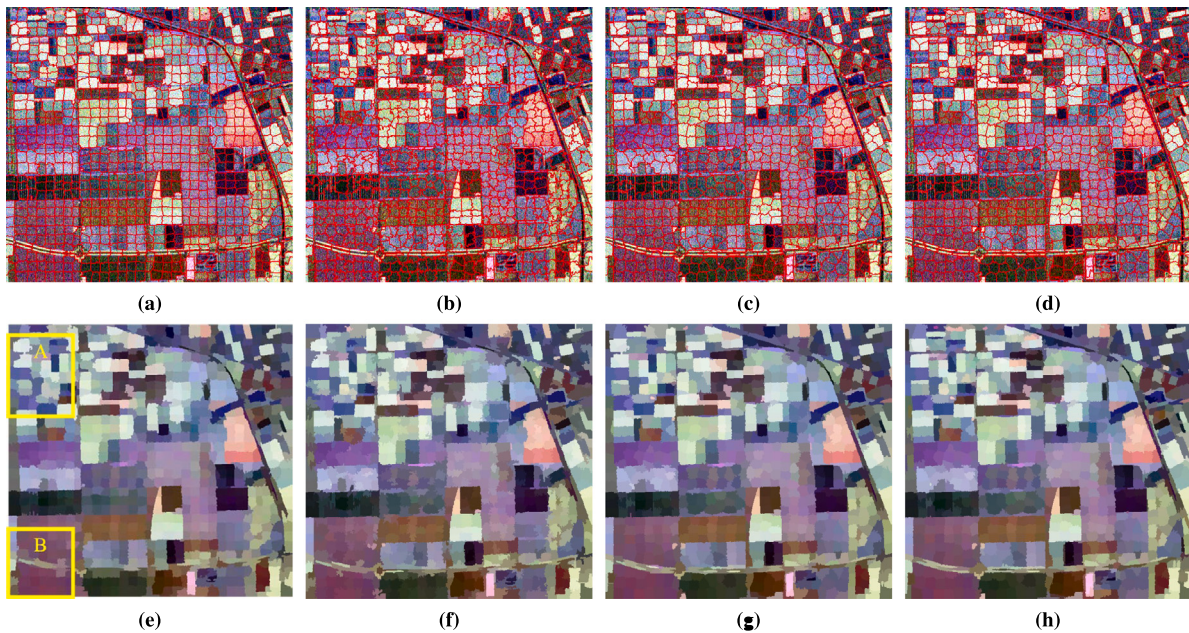


Fig. 14. Line graphs of evaluation metrics for four methods on GF-3 data at different numbers of superpixels: (a) BR; (b) ASA.

all four methods achieve good segmentation results. However, when zooming in on the yellow rectangular area A and plotting the results in Fig. 16(a)–(d), it can be seen that the edge adherence performance of the Qin-RW and Yin-HLT methods is poor. The superpixels segmented by these two methods do not adhere well to the edges and corners of the rectangular farmland area, missing many real boundaries. In contrast, the proposed methods retains these edge and corner features well, and the generated superpixels are regular. Furthermore, when zooming in on the area B marked with yellow rectangle and comparing the results in Fig. 16(e)–(h), it is found that the proposed method better preserves the edge information of narrow strip areas, and the edges of the superpixels are smoother and closer to the real edges.

Similar to the previous sections, we set the step size to a range of different values to quantitatively compare the performance of various methods on AIRSAR data. The experimental results are plotted in Fig. 17. It can be observed that the proposed method significantly outperforms the Qin-RW and Yin-HLT methods in both BR and ASA. When the step size  $S$  is 42, compared to the Qin-RW and Yin-HLT methods, the ASLIC method improves BR by 11.07% and 4.72%, respectively, and ASA by 7.99% and 5.65%, respectively. After introducing the multiscale initialization step, the number of superpixels increases from 182 to 207, but the improvement in BR becomes 16.56% and 10.21%, respectively, and in ASA becomes 12.01% and 9.67%, respectively. This indicates that the multiscale initialization method can significantly enhance BR and ASA at a relatively low cost. Furthermore, in this set of experiments, the Qin-RW method achieves the highest BR value of 92.82% when the number of superpixels is 3480. From the auxiliary line in Fig. 17, it can be seen that the MS-ASLIC method can reach



**Fig. 15.** Superpixel results of four methods on AIRSAR data when  $S = 19$ . (a), (e) Qin-RW; (b), (f) Yin-HLT; (c), (g) ASLIC; (d), (h) MS-ASLIC.

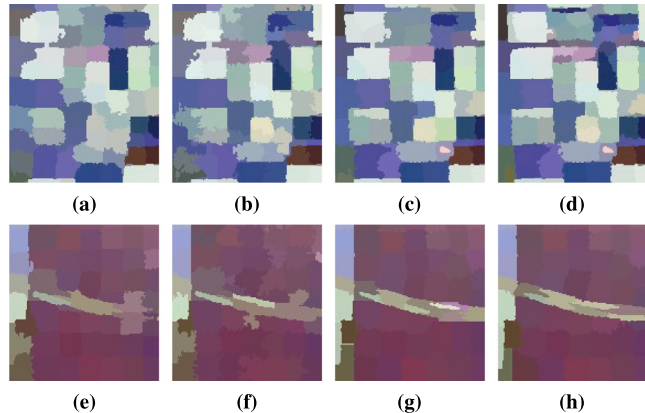


**Fig. 16.** Superpixel generation results of the area A and B marked with yellow rectangle in Fig. 15. (a), (e) Qin-RW; (b), (f) Yin-HLT; (c), (g) ASLIC; (d), (h) MS-ASLIC.

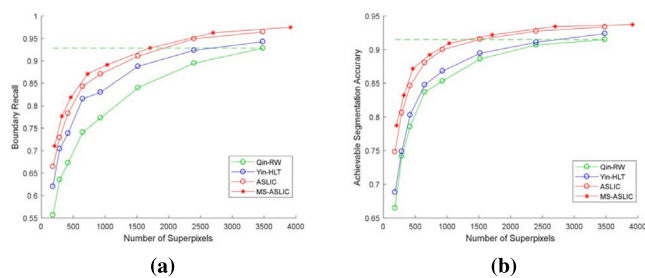


**Fig. 17.** Line graphs of evaluation metrics for four methods on AIRSAR data at different numbers of superpixels: (a) BR; (b) ASA.

this value with only 1710 superpixels. For ASA, the MS-ASLIC method can achieve the highest value (91.50%) of the Qin-RW method with approximately 1364 superpixels. This means that, for this dataset, the MS-ASLIC method can achieve equivalent or even better segmentation results with only half the number of superpixels required by the Qin-RW method.

#### 4.4. Performance of in large-scale scenes

As shown in Fig. 18, experiments were conducted on three diverse large-scale PolSAR datasets to demonstrate the robustness of the proposed algorithm. Among them, Fig. 18(a) was collected by the GF-3 C-band system over Paris, France, with an image size of  $4000 \times 3200$  and azimuth and range resolutions of 4.2 m and 4.8 m, respectively. Figs. 18(b) and 18(c) were collected by the UAVSAR L-band system over New Orleans, USA, and New York City, USA, with both images having a size of  $3300 \times 4000$  and azimuth and range resolutions of 7.2 m and 5.0 m, respectively. The step size for the proposed algorithm was set to 20, with other parameters being the same as those mentioned above. The superpixel segmentation results obtained by the proposed algorithm are shown in Fig. 18(d)–(f), where the upper half of the images shows superpixel boundaries overlaid on the Pauli images, and the lower half is obtained by replacing each pixel with the average value of its corresponding superpixel. Representative regions from the three large-scale scenes are selected, and the superpixel segmentation results are zoomed in and presented in Figs. 19–21 for further analysis.

**GF-3 Paris Data:** As shown in Fig. 18(a), the main land covers in the data include urban buildings, vegetation, and river. From the superpixel results in Fig. 18(d), it is clear that the edges of river, roads, and bridges are well preserved. We selected four regions ( $200 \times 200$ ) for zooming in and plotted them in Fig. 19. The main land covers of the four regions are as follows: A: vegetation, B: buildings, C: river and bridge, D: river and island. The results show that the algorithm generates compact superpixels in the homogeneous vegetation region and effectively preserves the edge details of buildings, bridges and river.

**UAVSAR New Orleans Data:** As shown in Fig. 18(b), the main land covers in this data include urban buildings, ocean, rivers, wetlands, and vegetation. From Fig. 18(e), it is clear that the edges of the coast, riverbanks, roads, and bridges are well preserved. We selected five representative regions ( $200 \times 200$ ) for zooming in and plotted them in Fig. 20. The main land covers of the five regions are as follows: A: vegetation and roads, B: ocean and bridge, C: urban buildings and roads, D: river delta and ships, E: wetlands. From the experimental results in Fig. 20, it can be observed that the proposed algorithm achieves robust results across different regions. The detailed information of the land covers in various scenes is well extracted, and even narrow roads and water features are preserved to some extent.

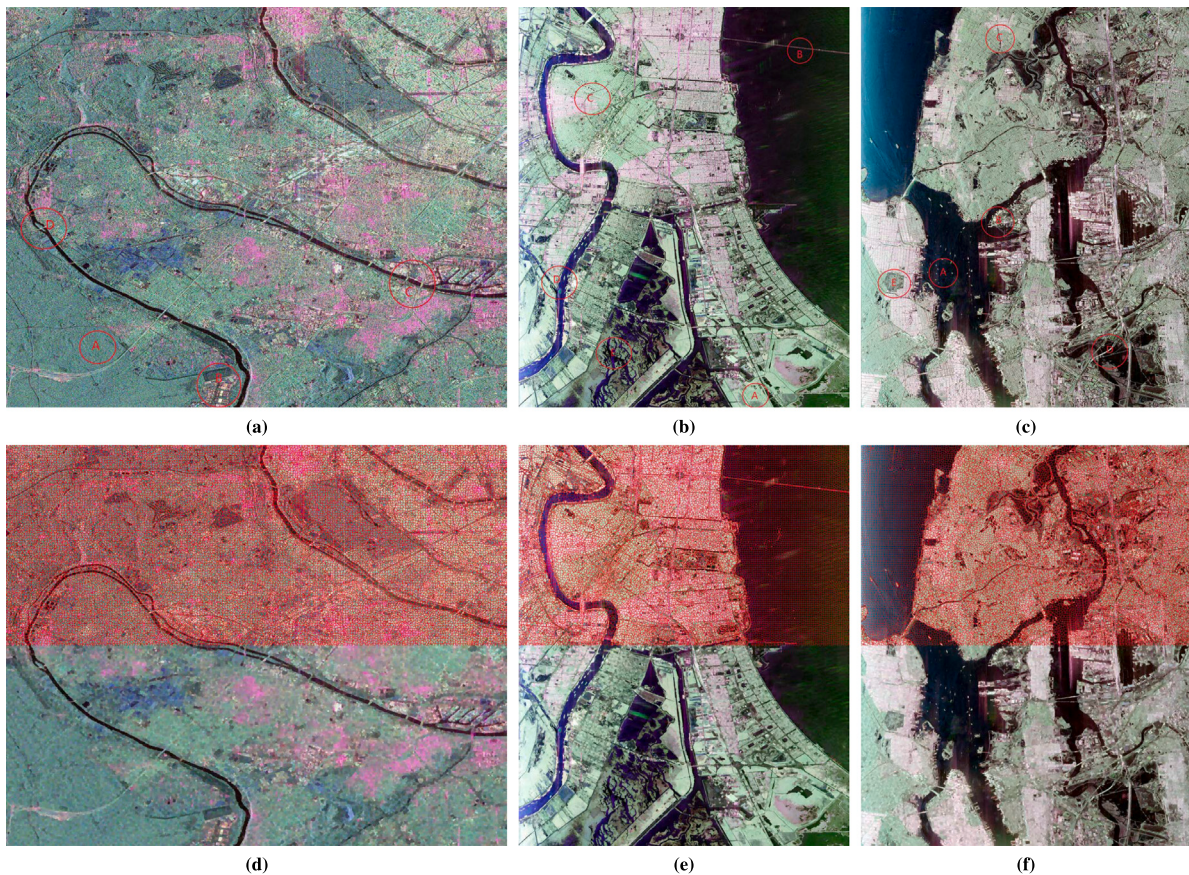


**Fig. 18.** Pauli image and corresponding superpixel results of proposed method on three large-scale scenes. (a) and (d) GF-3 Paris Data; (b) and (e) UAVSAR New Orleans Data; (c) and (f) UAVSAR New York Data.

**UAVSAR New York Data:** As shown in Fig. 18(c), the main land covers in this dataset include ocean, rivers, urban buildings, and a small amount of vegetation. From Fig. 18(f), it can be observed that the edges of ships, ports, rivers, and bridges are well extracted. Five representative regions ( $200 \times 200$ ) were selected, zoomed in, and plotted in Fig. 21. The main land covers of these regions are as follows: A: ocean and ships, B: port, C: buildings and roads, D: bridges and river, E: vegetation. The results show that the details of smaller targets, such as ships and ports, which are significantly smaller than the step size, are well preserved. Additionally, the details of narrow roads and bridges remain well represented in the superpixel segmentation results.

#### 4.5. Performance of multiscale initialization method

To demonstrate the effectiveness of the proposed multi-scale initialization method, this section compares the performances of the Qin-RW method, the Yin-HLT method, and the proposed method under different step sizes and different initialization steps. Similar to the experiments in the previous section, we set the step sizes to a range of values from large to small, specifically  $S = [42, 34, 28, 23, 19, 15, 12, 10]$ . The initialization steps for the three methods are configured as the original method and the proposed multiscale initialization method. The ASA and BR performances for the three datasets are presented in Tables 1 to 6, where MS-Qin-RW indicates the Qin-RW method combined with the proposed multiscale initialization step, and MS-Yin-HLT indicates the Yin-HLT method combined with the proposed multiscale initialization step. Overall, when the initialization methods are the same, the proposed method consistently outperforms both the Qin-RW and Yin-HLT methods in terms of ASA and BR across the three datasets. Furthermore, the introduction of the multiscale initialization step leads to varying degrees of improvement in ASA and BR for all three methods.

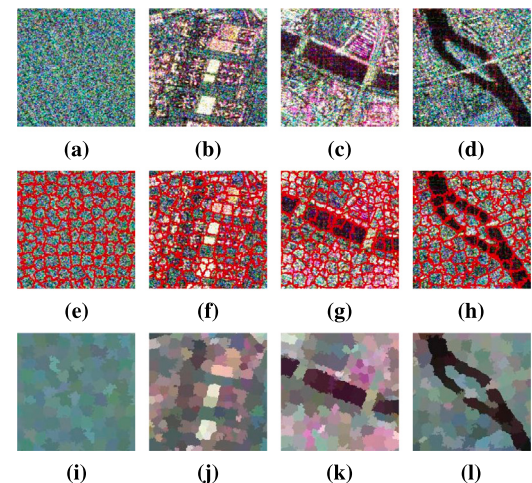


**Fig. 19.** Zoom-in view of the 4 selected regions on GF-3 Paris Data.

**EMISAR Data:** Tables 1 and 2 present the ASA and BR performances for the EMISAR data. It can be observed that after introducing the multiscale initialization step, the ASA and BR of the Qin-RW method improved by an average of 0.97% and 2.66%, respectively. When the step size is 42, the ASA increased by a maximum of 1.78%, and when the step size is 34, the BR increased by a maximum of 4.78%. For the Yin-HLT method, the introduction of the multi-scale initialization step resulted in average improvements of 1.63% and 3.39% in ASA and BR, respectively. At a step size of 42, the ASA saw a maximum increase

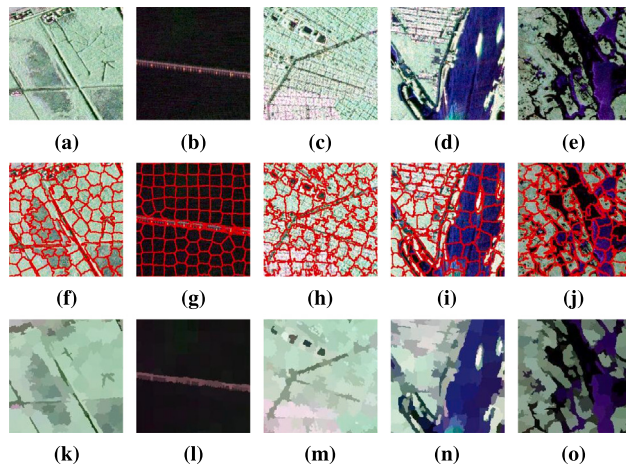


Fig. 20. Zoom-in view of the 5 selected regions on UAVSAR New Orleans Data.

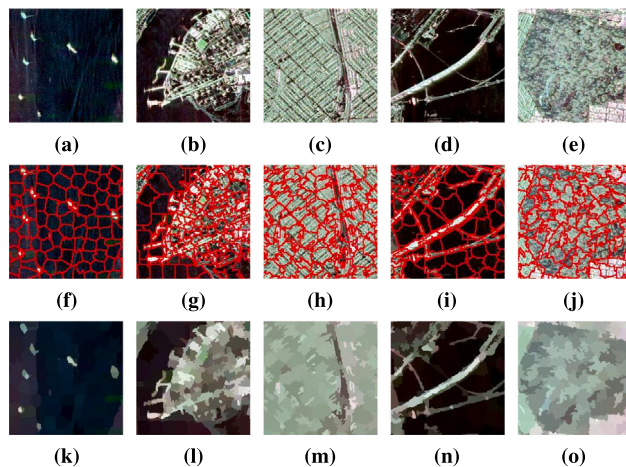


Fig. 21. Zoom-in view of the 5 selected regions on UAVSAR New York Data.

Table 1

ASA for the six methods on EMISAR data at different numbers of superpixels.

Superpixels Numbers	196	289	441	650	961	1521	2401	3422
Qin-RW	0.7229	0.7674	0.8070	0.8385	0.8641	0.8873	0.9042	0.9152
Yin-HLT	0.7153	0.7644	0.8049	0.8338	0.8582	0.8848	0.9060	0.9149
ASLIC	0.7241	0.7827	0.8235	0.8500	0.8748	0.8954	0.9126	0.9213
Superpixels Numbers	221	321	497	731	1074	1712	2699	3841
MS-Qin-RW	0.7406	0.7775	0.8226	0.8488	0.8725	0.8933	0.9103	0.9187
MS-Yin-HLT	0.7509	0.7772	0.8256	0.8572	0.8720	0.8947	0.9136	0.9215
MS-ASLIC	0.7458	0.8038	0.8398	0.8691	0.8906	0.9061	0.9206	0.9272

of 3.56%, and at a step size of 28, the BR had a maximum increase of 5.91%. For the proposed method, the introduction of the multiscale initialization step led to average improvements of 1.48% and 3.52% in ASA and BR, respectively. When the step size is 42, the ASA reached a maximum increase of 2.17%, and when the step size is 28, the BR achieved a maximum increase of 5.89%.

**GF-3 Data:** Tables 3 and 4 present the ASA and BR performances for the GF-3 data. It can be observed that after introducing the multiscale initialization step, the ASA and BR of the Qin-RW method improved by an average of 0.66% and 5.49%, respectively. When the step size is 34, the ASA reached a maximum increase of 0.99%, while the BR saw a maximum increase of 7.20%. For the Yin-HLT method, the introduction of the multiscale initialization step resulted in average improvements of 0.60% and 4.01% in ASA and BR, respectively. At a step size of

Table 2

BR for the six methods on EMISAR data at different numbers of superpixels.

Superpixels Numbers	196	289	441	650	961	1521	2401	3422
Qin-RW	0.6237	0.6694	0.7379	0.7939	0.8595	0.9053	0.9414	0.9641
Yin-HLT	0.6487	0.6848	0.7443	0.8061	0.9642	0.9051	0.9498	0.9680
ASLIC	0.6401	0.7057	0.7647	0.8176	0.8816	0.9181	0.9553	0.9746
Superpixels Numbers	221	321	497	731	1074	1712	2699	3841
MS-Qin-RW	0.6513	0.7172	0.7843	0.8315	0.8759	0.9229	0.9554	0.9695
MS-Yin-HLT	0.6787	0.7338	0.8034	0.8562	0.8925	0.9367	0.9652	0.9755
MS-ASLIC	0.6886	0.7613	0.8236	0.8600	0.9062	0.9462	0.9713	0.9821

Table 3

ASA for the six methods on GF-3 data at different numbers of superpixels.

Superpixels Numbers	378	572	864	1287	1880	3060	4725	6840
Qin-RW	0.9185	0.9247	0.9339	0.9420	0.9460	0.9553	0.9605	0.9650
Yin-HLT	0.9096	0.9198	0.9294	0.9395	0.9453	0.9543	0.9596	0.9649
ASLIC	0.9194	0.9309	0.9392	0.9483	0.9518	0.9580	0.9652	0.9687
Superpixels Numbers	428	647	979	1453	2120	3450	5327	7695
MS-Qin-RW	0.9249	0.9346	0.9407	0.9480	0.9535	0.9608	0.9660	0.9699
MS-Yin-HLT	0.9154	0.9286	0.9355	0.9427	0.9516	0.9611	0.9652	0.9701
MS-ASLIC	0.9301	0.9372	0.9441	0.9531	0.9590	0.9647	0.9683	0.9720

Table 4

BR for the six methods on GF-3 data at different numbers of superpixels.

Superpixels Numbers	378	572	864	1287	1880	3060	4725	6840
Qin-RW	0.5562	0.6131	0.6620	0.7172	0.7754	0.8279	0.8865	0.9302
Yin-HLT	0.5809	0.6288	0.6929	0.7524	0.7997	0.8681	0.9101	0.9529
ASLIC	0.6153	0.6706	0.7176	0.7650	0.8193	0.8730	0.9261	0.9547
Superpixels Numbers	428	647	979	1453	2120	3450	5327	7695
MS-Qin-RW	0.6097	0.6851	0.7312	0.7847	0.8281	0.8791	0.9285	0.9620
MS-Yin-HLT	0.6162	0.6690	0.7477	0.8031	0.8555	0.9052	0.9413	0.9690
MS-ASLIC	0.6640	0.7257	0.7767	0.8135	0.8652	0.9138	0.9496	0.9741

34, the ASA achieved a maximum increase of 0.88%, and at a step size of 19, the BR reached a maximum increase of 5.58%. For the proposed method, the introduction of the multiscale initialization step led to average improvements of 0.59% and 4.26% in ASA and BR, respectively. When the step size is 42, the ASA saw a maximum increase of 1.07%, and at a step size of 28, the BR achieved a maximum increase of 5.92%.

**AIRSAR Data:** Tables 5 and 6 present the ASA and BR performances for the AIRSAR data. It can be observed that after introducing the multiscale initialization step, the ASA and BR of the Qin-RW method improved by an average of 1.75% and 4.83%, respectively. When the step size is 42, the ASA reached a maximum increase of 3.00%, while the BR saw a maximum increase of 7.91%. For the Yin-HLT method, the introduction of the multi-scale initialization step resulted in average improvements of 1.49% and 3.18% in ASA and BR, respectively. At a step size of 42, the ASA had a maximum increase of 2.93%, and the BR achieved a maximum increase of 5.53%. For the proposed method, the introduction of the multi-scale initialization step led to average improvements of 1.81% and 3.12% in ASA and BR, respectively. When the step size is 42, the ASA saw a maximum increase of 4.02%, and at a step size of 34, the BR had a maximum increase of 5.49%.

## 5. Conclusion

This paper presents a multiscale adaptive superpixel generation method for PolSAR images, implemented within the SLIC framework. Key contributions include a polarimetric scattering feature similarity measure, a multiscale initialization method for cluster centers, and an adaptive clustering distance measure. The polarimetric scattering feature similarity, derived from polarimetric target decomposition, accurately reflects land cover features and excels in heterogeneous urban

**Table 5**

ASA for the six methods on AIRSAR data at different numbers of superpixels.

Superpixels Numbers	182	289	420	650	930	1520	2400	3480
Superpixels Numbers	0.6648	0.7417	0.7855	0.8370	0.8534	0.8862	0.9068	0.9150
Yin-HLT	0.6882	0.7488	0.8029	0.8476	0.8682	0.8945	0.9109	0.9239
ASLIC	0.7447	0.8125	0.8416	0.8789	0.8984	0.9149	0.9310	0.9342
Superpixels Numbers	207	322	463	727	1034	1710	2700	3915
MS-Qin-RW	0.6948	0.7626	0.8077	0.8553	0.8703	0.8991	0.9171	0.9235
MS-Yin-HLT	0.7175	0.7728	0.8228	0.8648	0.8760	0.9036	0.9173	0.9298
MS-ASLIC	0.7849	0.8357	0.8679	0.9029	0.9081	0.9263	0.9353	0.9399

**Table 6**

BR for the six methods on AIRSAR data at different numbers of superpixels.

Superpixels Numbers	182	289	420	650	930	1520	2400	3480
Qin-RW	0.5565	0.6352	0.6725	0.7407	0.7726	0.8402	0.8947	0.9282
Yin-HLT	0.6200	0.7039	0.7387	0.8156	0.8300	0.8878	0.94235	0.9426
ASLIC	0.6672	0.7419	0.7899	0.8547	0.8829	0.9194	0.9549	0.9709
Superpixels Numbers	207	322	463	727	1034	1710	2700	3915
MS-Qin-RW	0.6256	0.6886	0.7262	0.7916	0.8192	0.8784	0.9321	0.9551
MS-Yin-HLT	0.6754	0.7431	0.7781	0.8469	0.8582	0.9131	0.9444	0.9570
MS-ASLIC	0.7221	0.7810	0.8279	0.8906	0.9030	0.9510	0.9713	0.9847

areas. The multiscale initialization enhances information extraction by allocating more superpixels to heterogeneous regions, while the adaptive clustering distance measure combines multiple features for optimized clustering. Experimental results demonstrate that our method outperforms existing approaches, providing more regular superpixels in homogeneous areas and capturing finer details in heterogeneous regions. This capability enhances applications like land cover classification and urban monitoring. Further investigation is needed regarding the variability of polarimetric target decomposition methods and the manual tuning of initialization parameters. Future research could focus on adaptive parameter settings to optimize performance across diverse datasets.

#### CRediT authorship contribution statement

**Nengcai Li:** Writing – original draft, Methodology, Investigation. **Deliang Xiang:** Writing – review & editing, Supervision, Methodology. **Xiaokun Sun:** Software, Resources, Formal analysis. **Canbin Hu:** Validation, Investigation, Formal analysis. **Yi Su:** Visualization, Supervision, Resources.

#### Declaration of competing interest

The authors declare that they have no known competing financial interests or personal relationships that could have appeared to influence the work reported in this paper.

#### Acknowledgment

This research was supported by [National Natural Science Foundation of China] under Grant ID [62171015].

#### References

- Achanta, R., Shaji, A., Smith, K., Lucchi, A., Fua, P., Süsstrunk, S., 2012. SLIC superpixels compared to state-of-the-art superpixel methods. *IEEE Trans. Pattern Anal. Mach. Intell.* **34** (11), 2274–2282.
- Alonso, A., López, C., Papathanassiou, K., Hajnsek, I., 2020. Polarimetric SAR time series change analysis over agricultural areas. *IEEE Trans. Geosci. Remote Sens.* **58** (10), 7317–7330. <http://dx.doi.org/10.1109/TGRS.2020.2981929>, URL <http://hdl.handle.net/2117/338190>.
- An, W., Xie, C., Lin, M., 2016. A three-component decomposition algorithm for polarimetric SAR with the helix angle compensation. In: 2016 IEEE International Geoscience and Remote Sensing Symposium. IEEE, pp. 7501–7504.
- Anfinsen, S.N., Doulgeris, A.P., Eltoft, T.r., 2009. Estimation of the equivalent number of looks in polarimetric synthetic aperture radar imagery. *IEEE Trans. Geosci. Remote Sens.* **47** (11), 3795–3809.
- Barcelos, I.B., Belém, F.D.C., João, L.D.M., Patrocínio Jr., Z.K.D., Falcão, A.X., Guimarães, S.J.F., 2024. A comprehensive review and new taxonomy on superpixel segmentation. *ACM Comput. Surv.* **56** (8), 1–39.
- Cherian, A., Sra, S., Banerjee, A., Papankolopoulos, N., 2012. Jensen-bregman logdet divergence with application to efficient similarity search for covariance matrices. *IEEE Trans. Pattern Anal. Mach. Intell.* **35** (9), 2161–2174.
- Comaniciu, D., Meer, P., 2002. Mean shift: A robust approach toward feature space analysis. *IEEE Trans. Pattern Anal. Mach. Intell.* **24** (5), 603–619.
- Deng, J., Wang, W., Zhang, H., Zhang, T., Zhang, J., 2024. PolSAR ship detection based on superpixel-level contrast enhancement. *IEEE Geosci. Remote Sens. Lett.*
- Feng, J., Cao, Z., Pi, Y., 2014. Polarimetric contextual classification of PolSAR images using sparse representation and superpixels. *Remote Sens.* **6** (8), 7158–7181.
- Freeman, A., Durden, S.L., 1998. A three-component scattering model for polarimetric SAR data. *IEEE Trans. Geosci. Remote Sens.* **36** (3), 963–973.
- Gao, H., Wang, C., Xiang, D., Ye, J., Wang, G., 2021. TSPol-ASLIC: Adaptive superpixel generation with local iterative clustering for time-series quad-and dual-polarization SAR data. *IEEE Trans. Geosci. Remote Sens.* **60**, 1–15.
- Garg, R., Kumar, A., Bansal, N., Prateek, M., Kumar, S., 2021. Semantic segmentation of PolSAR image data using advanced deep learning model. *Sci. Rep.* **11** (1), 15365.
- Ge, P., Gokon, H., Meguro, K., 2020. A review on synthetic aperture radar-based building damage assessment in disasters. *Remote Sens. Environ.* **240**, 111693.
- Greco, M.S., Gini, F., 2007. Statistical analysis of high-resolution SAR ground clutter data. *IEEE Trans. Geosci. Remote Sens.* **45** (3), 566–575.
- Guo, Y., Jiao, L., Qu, R., Sun, Z., Wang, S., Wang, S., Liu, F., 2022. Adaptive fuzzy learning superpixel representation for PolSAR image classification. *IEEE Trans. Geosci. Remote Sens.* **60**.
- Hu, C., Wang, Y., Sun, X., Quan, S., Xiang, D., 2023. Model-based polarimetric target decomposition with power redistribution for urban areas. *IEEE J. Sel. Top. Appl. Earth Obs. Remote Sens.*
- Hu, S., Xie, Q., Ballester-Berman, J.D., Dou, Q., Peng, X., Wang, Y., Fu, H., Zhu, J., 2024. A general three-component polarimetric SAR interferometry target decomposition. *Adv. Space Res.* **74** (11), 5428–5437.
- Levinstein, A., Stere, A., Kutulakos, K.N., Fleet, D.J., Dickinson, S.J., Siddiqi, K., 2009. Turbopixels: Fast superpixels using geometric flows. *IEEE Trans. Pattern Anal. Mach. Intell.* **31** (12), 2290–2297.
- Li, N., Hu, C., Wang, W., Quan, S., Xiang, D., 2023a. Polarimetric SAR target decomposition method based on independent polarization orientation angle integration. *Acta Geod. Cartograph. Sin.* **52** (12), 2141–2153. <http://dx.doi.org/10.11947/j.AGCS.2023.20220552>.
- Li, X., Yan, L., Qi, P., Zhang, L., Goudail, F., Liu, T., Zhai, J., Hu, H., 2023b. Polarimetric imaging via deep learning: A review. *Remote Sens.* **15** (6), 1540.
- Li, M., Zou, H., Qin, X., Dong, Z., Sun, L., Wei, J., 2022. Efficient superpixel generation for polarimetric SAR images with cross-iteration and hexagonal initialization. *Remote Sens.* **14** (12), 2914.
- Li, M., Zou, H., Qin, X., Dong, Z., Sun, L., Wei, J., 2023c. Superpixel generation for polarimetric SAR images with adaptive size estimation and determinant ratio test distance. *Remote Sens.* **15** (4), 1123.
- Liu, F., Duan, Y., Li, L., Jiao, L., Wu, J., Yang, S., Zhang, X., Yuan, J., 2016. SAR image segmentation based on hierarchical visual semantic and adaptive neighborhood multinomial latent model. *IEEE Trans. Geosci. Remote Sens.* **54** (7), 4287–4301.
- Liu, M.-Y., Tuzel, O., Ramalingam, S., Chellappa, R., 2011. Entropy rate superpixel segmentation. In: CVPR 2011. IEEE, pp. 2097–2104.
- Liu, B., Zhang, Z., Liu, X., Yu, W., 2014. Edge extraction for polarimetric SAR images using degenerate filter with weighted maximum likelihood estimation. *IEEE Geosci. Remote Sens. Lett.* **11** (12), 2140–2144.
- Moakher, M., Batchelor, P.G., 2006. Symmetric positive-definite matrices: From geometry to applications and visualization. In: *Visualization and Processing of Tensor Fields*. Springer, pp. 285–298.
- Moore, A.P., Prince, S.J., Warrell, J., Mohammed, U., Jones, G., 2008. Superpixel lattices. In: 2008 IEEE Conference on Computer Vision and Pattern Recognition. IEEE, pp. 1–8.
- Parida, B.R., Mandal, S.P., 2020. Polarimetric decomposition methods for LULC mapping using ALOS L-band PolSAR data in Western parts of Mizoram, Northeast India. *SN Appl. Sci.* **2** (6), 1049.
- Pennec, X., Fillard, P., Ayache, N., 2006. A Riemannian framework for tensor computing. *Int. J. Comput. Vis.* **66**, 41–66.
- Qin, F., Guo, J., Lang, F., 2014. Superpixel segmentation for polarimetric SAR imagery using local iterative clustering. *IEEE Geosci. Remote Sens. Lett.* **12** (1), 13–17.
- Qin, X., Zhang, Y., Li, Y., Cheng, Y., Yu, W., Wang, P., Zou, H., 2022. Distance measures of polarimetric SAR image data: A survey. *Remote Sens.* **14** (22), 5873.
- Quan, S., Zhang, T., Wang, W., Kuang, G., Wang, X., Zeng, B., 2023a. Exploring fine polarimetric decomposition technique for built-up area monitoring. *IEEE Trans. Geosci. Remote Sens.* **61**, 1–19.
- Quan, S., Zhang, T., Wang, W., Kuang, G., Wang, X., Zeng, B., 2023b. Exploring fine polarimetric decomposition technique for built-up area monitoring. *IEEE Trans. Geosci. Remote Sens.* **61**, 1–19. <http://dx.doi.org/10.1109/TGRS.2023.3257773>.

- Schou, J., Skriver, H., Nielsen, A.A., Conradsen, K., 2003. CFAR edge detector for polarimetric SAR images. *IEEE Trans. Geosci. Remote Sens.* 41 (1), 20–32.
- Shi, J., He, T., Ji, S., Nie, M., Jin, H., 2023. CNN-improved superpixel-to-pixel fuzzy graph convolution network for PolSAR image classification. *IEEE Trans. Geosci. Remote Sens.*.
- Shi, J., Malik, J., 2000. Normalized cuts and image segmentation. *IEEE Trans. Pattern Anal. Mach. Intell.* 22 (8), 888–905.
- Shi, C., Pun, C.-M., 2019. Multiscale superpixel-based hyperspectral image classification using recurrent neural networks with stacked autoencoders. *IEEE Trans. Multimed.* 22 (2), 487–501.
- Shui, P.-L., Cheng, D., 2012. Edge detector of SAR images using Gaussian-Gamma-shaped bi-windows. *IEEE Geosci. Remote Sens. Lett.* 9 (5), 846–850.
- Silva-Perez, C., Marino, A., Lopez-Sanchez, J.M., Cameron, I., 2021. Multitemporal polarimetric SAR change detection for crop monitoring and crop type classification. *IEEE J. Sel. Top. Appl. Earth Obs. Remote Sens.* 14, 12361–12374.
- Singh, G., Yamaguchi, Y., 2018. Model-based six-component scattering matrix power decomposition. *IEEE Trans. Geosci. Remote Sens.* 56 (10), 5687–5704.
- Song, H., Yang, W., Bai, Y., Xu, X., 2015. Unsupervised classification of polarimetric SAR imagery using large-scale spectral clustering with spatial constraints. *Int. J. Remote Sens.* 36 (11), 2816–2830.
- Sun, Q., Liu, M., Chen, S., Lu, F., Xing, M., 2023. Ship detection in SAR images based on multilevel superpixel segmentation and fuzzy fusion. *IEEE Trans. Geosci. Remote Sens.* 61, 1–15.
- Vedaldi, A., Soatto, S., 2008. Quick shift and kernel methods for mode seeking. In: Computer Vision–ECCV 2008: 10th European Conference on Computer Vision, Marseille, France, October 12–18, 2008, Proceedings, Part IV 10. Springer, pp. 705–718.
- Vincent, L., Soille, P., 1991. Watersheds in digital spaces: an efficient algorithm based on immersion simulations. *IEEE Trans. Pattern Anal. Mach. Intell.* 13 (06), 583–598.
- Wang, R., Nie, Y., Geng, J., 2024. Multiscale superpixel-guided weighted graph convolutional network for polarimetric SAR image classification. *IEEE J. Sel. Top. Appl. Earth Obs. Remote Sens.*.
- Xiang, D., Ban, Y., Wang, W., Su, Y., 2017. Adaptive superpixel generation for polarimetric SAR images with local iterative clustering and SIRV model. *IEEE Trans. Geosci. Remote Sens.* 55 (6), 3115–3131.
- Xiang, D., Wang, W., Tang, T., Guan, D., Quan, S., Liu, T., Su, Y., 2019. Adaptive statistical superpixel merging with edge penalty for PolSAR image segmentation. *IEEE Trans. Geosci. Remote Sens.* 58 (4), 2412–2429.
- Xie, L., Zhang, H., Wang, C., Liu, M., Zhang, B., 2015. Superpixel-based PolSAR images change detection. In: 2015 IEEE 5th Asia-Pacific Conference on Synthetic Aperture Radar. APSAR, IEEE, pp. 792–796.
- Xu, D., Li, M., Wu, Y., Zhang, P., Xin, X., Yang, Z., 2023. Difference-guided multiscale graph convolution network for unsupervised change detection in PolSAR images. *Neurocomputing* 555, 126611.
- Yamaguchi, Y., Sato, A., Boerner, W.-M., Sato, R., Yamada, H., 2011. Four-component scattering power decomposition with rotation of coherency matrix. *IEEE Trans. Geosci. Remote Sens.* 49 (6), 2251–2258.
- Ye, J., Wang, C., Gao, H., Fan, H., Song, T., Ding, L., 2022. A novel unsupervised object-level crop rotation detection with time-series dual-polarimetric SAR data. *IEEE Geosci. Remote Sens. Lett.* 19, 1–5.
- Yin, J., Wang, T., Du, Y., Liu, X., Zhou, L., Yang, J., 2021. SLIC superpixel segmentation for polarimetric SAR images. *IEEE Trans. Geosci. Remote Sens.* 60, 1–17.
- Zhang, S., Li, S., Fu, W., Fang, L., 2017. Multiscale superpixel-based sparse representation for hyperspectral image classification. *Remote Sens.* 9 (2), 139.
- Zhang, F., Sun, X., Ma, F., Yin, Q., 2024a. Superpixelwise likelihood ratio test statistic for PolSAR data and its application to built-up area extraction. *ISPRS J. Photogramm. Remote Sens.* 209, 233–248.
- Zhang, F., Sun, X., Ma, F., Yin, Q., 2024b. Superpixelwise likelihood ratio test statistic for PolSAR data and its application to built-up area extraction. *ISPRS J. Photogramm. Remote Sens.* 209, 233–248.
- Zou, B., Xu, X., Zhang, L., 2020. Object-based classification of PolSAR images based on spatial and semantic features. *IEEE J. Sel. Top. Appl. Earth Obs. Remote Sens.* 13, 609–619.